Neurochemical Research (2023) 48:2360–2389
https://doi.org/10.1007/s11064-023-03907-x

ORIGINAL PAPER

Mitochondrial Complex I Inhibition in Dopaminergic Neurons Causes Altered Protein Profile and Protein Oxidation: Implications for Parkinson's disease

Yogeshachar Chithra[1] · Gourav Dey[2] · Vivek Ghose[3] · Vivek Chandramohan[4] · Niya Gowthami[5] · V. Vasudev[1] · M. M. Srinivas Bharath[5]

Received: 21 November 2022 / Revised: 25 February 2023 / Accepted: 3 March 2023 / Published online: 25 March 2023

Abstract

Mitochondrial dysfunction and oxidative stress are critical to neurodegeneration in Parkinson's disease (PD). Mitochondrial dysfunction in PD entails inhibition of the mitochondrial complex I (CI) in the dopaminergic neurons of substantia nigra. The events contributing to CI inhibition and downstream pathways are not completely elucidated. We conducted proteomic analysis in a dopaminergic neuronal cell line exposed individually to neurotoxic CI inhibitors: rotenone (Rot), paraquat (Pq) and 1-methyl-4-phenylpyridinium (MPP^+). Mass spectrometry (MS) revealed the involvement of biological processes including cell death pathways, structural changes and metabolic processes among others, most of which were common across all models. The proteomic changes induced by Pq were significantly higher than those induced by Rot and MPP^+. Altered metabolic processes included downregulated mitochondrial proteins such as CI subunits. MS of CI isolated from the models revealed oxidative post-translational modifications with Tryptophan (Trp) oxidation as the predominant modification. Further, 62 peptides in 22 subunits of CI revealed Trp oxidation with 16 subunits common across toxins. NDUFV1 subunit had the greatest number of oxidized Trp and Rot model displayed the highest number of Trp oxidation events compared to the other models. Molecular dynamics simulation (MDS) of NDUFV1 revealed that oxidized Trp 433 altered the local conformation thereby changing the distance between the Fe-S clusters, Fe-S 301(N1a) to Fe-S 502 (N3) and Fe-S 802 (N4) to Fe-S 801 (N5), potentially affecting the efficiency of electron transfer. The events triggered by the neurotoxins represent CI damage, mitochondrial dysfunction and neurodegeneration in PD.

Keywords Rotenone · Paraquat · MPP^+ (1-methyl-4-phenylpyridinium) · Mass spectrometry · Tryptophan · Post-translational Modifications · Molecular dynamics

Introduction

Mitochondrial dysfunction and oxidative damage are central to the neurodegeneration and pathogenesis of Parkinson's disease (PD). Research evidences from human postmortem brain samples have revealed that mitochondrial damage in the substantia nigra region of PD patients mainly includes inhibition of mitochondrial complex I (CI) [1–3].

CI is the first enzyme of the electron transport chain with 44 subunits and molecular weight of ~1 MD. Defect in CI activity has been reported in human diseases [4]. Studies on patient samples from mitochondrial disorders have revealed that specific genetic mutations in different subunits of the complex could potentially contribute to the lowered enzyme activity [5]. Apart from this, post-translational modifications (PTMs) of the CI subunits could potentially alter the

✉ M. M. Srinivas Bharath
bharath@nimhans.ac.in; thathachar2010@gmail.com

[1] Department of Bioscience, P.G. Center, Hemagangotri, University of Mysore, Hassan, Karnataka 573220, India

[2] Institute of Bioinformatics, International Tech Park, Bangalore 560066, India

[3] Manipal Academy of Higher Education, Udupi, Karnataka 576104, India

[4] Department of Biotechnology, Siddaganga Institute of Technology, Tumkur, Karnataka 572103, India

[5] Department of Clinical Psychopharmacology and Neurotoxicology, National Institute of Mental Health and Neurosciences (NIMHANS), No. 2900, Hosur Road, Lakkasandra, Bangalore 560029, India

structure–function relationship of CI [6]. PTMs are known to regulate protein structure and the associated biochemical pathways. PTMs could either be non-oxidative PTMs such as phosphorylation, acetylation, methylation or oxidative PTMs such as Tryptophan (Trp) and Cysteine (Cys) oxidation, Tyrosine (Tyr) nitration among others. Many PTMs that affect the function of mitochondrial proteins have been noted [6]. The CI subunits are also known to undergo PTMs during normal physiological condition and diseases. Studies on CI in different paradigms have extensively reported oxidative and non-oxidative PTMs [6, 7].

Epidemiological studies have indicated that exposure to toxic chemicals such as pesticides, herbicides and other neurotoxins could potentially induce acute PD or parkinsonism in humans [8]. Most of these neurotoxins such as rotenone (Rot), paraquat (Pq) and 1-methyl-4-phenylpyridinium (MPP^+) induced neurodegeneration via mitochondrial dysfunction and selective inhibition of CI [8]. Although these neurotoxic models have been used to study PD pathogenesis, certain questions remain unanswered. Firstly, whether the downstream pathways following exposure to these three toxins are comparable is not explored. Secondly, whether exposure to these three toxins can cause CI inhibition via oxidative damage of different subunits of the complex and whether these are common across the three models are largely unknown.

To address these lacunae, we have in this study compared the downstream pathways that are elicited following exposure to these three toxins in dopaminergic cell lines by carrying out a comprehensive proteomic analysis. We have also isolated CI from these three toxic models and compared the PTMs that could potentially characterize the inhibition of the complex. Finally, molecular dynamic simulation (MDS) approach was employed to understand the structural changes induced by selected oxidative PTMs in the critical subunits of the complex.

Materials and Methods

All the chemicals and solvents were of analytical grade. Routine and bulk chemicals were obtained from Sisco Research Laboratories (SRL) Pvt. Ltd. (Mumbai, Maharashtra, India). Fine chemicals such as Rot, Pq, MPP^+, 3-(4,5-dimethylthiazol-2-yl)-2,5-diphenyltetrazolium bromide (MTT), Dichlorodihydrofluorescein diacetate (DCF-DA), 5,5'-dithio-bis-(2-nitrobenzoic acid) (DTNB), Glutathione reductase and Anti-dinitrophenyl (DNP) antibody were obtained from Merck-Sigma (St. Louis, MO, USA). Cell culture consumables such as RPMI 1640, Trypsin EDTA from Merck-Sigma, Fetal Bovine serum from PAN Biotech (Aidenbach, Bavaria, Germany) and Antibiotic and antimycotic solution from HIMEDIA (Einhausen, Germany) were obtained. Primary antibodies (against VDAC1, β-actin, Biotin) and CI isolation/immunocapture kit were procured from Abcam (Cambridge, UK) (Cat No. ab109711). Anti-horseradish peroxidase conjugated secondary antibodies (anti-rabbit and anti-goat) were obtained from Bangalore Genei (Bangalore, Karnataka, India). Hydrazide biotin and TMT labelling kit were purchased from Thermo fisher scientific (Waltham, MA, USA). Sequencing grade modified trypsin was obtained from Promega (Madison, WI, USA). Mass spectrometry consumables such as sodium dodecyl sulphate (SDS), triethyl ammonium bicarbonate (TEABC) buffer, ammonium bicarbonate (ABC) buffer, iodoacetamide, dithiothreitol (DTT), acetone, formic acid (FA), acetonitrile (ACN) were obtained from Merck-Sigma.

Cell Culture

We have extensively used Rat dopaminergic 1RB3AN27 (N27) neuronal cell line throughout this study [9]. The cell line was obtained as a kind gift from Dr. Curt Freed, University of Colorado, USA. The cell line was cultured and maintained as previously described [10]. N27 cells were treated at different concentrations of Rot (0–2000 nM) or Pq (0–2000 μM) for 24 h and Rot (0–2000 nM) or Pq (0–200 μM) or MPP^+(0–2000 μM) for 48 h, assessed for cell viability using 3-(4,5-dimethylthiazol-2-yl)-2,5-diphenyltetrazolium bromide (MTT) assay [11] and LD_{25} and LD_{50} values were calculated at 48 h. (We have used LD_{25} and LD_{50} in all experiments except western blot experiments for mitochondrial samples and CI assay).

Alternately, Lactate dehydrogenase (LDH) assay was used to monitor cell viability [12] by measuring the activity in the culture supernatants of N27 cells treated with Rot (250 nM and 500 nM, 48 h), Pq (50 μM and 100 μM, 48 h) and MPP^+ (150 μM and 250 μM, 48 h). We have chosen different doses of each neurotoxins to measure LDH, because N27 showed varied sensitivity to the toxins in the MTT assay.

Measurement of Reactive Oxygen Species (ROS)

ROS generation in different neurotoxic models compared to the respective controls was assayed using dihydrodichloro fluorescein diacetate (H2 DCFH-DA) method as described [13].

Total Glutathione (GSH + GSSG) Estimation

The control and neurotoxin treated cells were subjected to total glutathione estimations by 5,5′-dithio-bis-2-nitrobenzoic acid (DTNB) recycling method [10, 13], based on the maximum reaction rate compared with GSSG standards (0–250 ng). All estimations were conducted in triplicate,

normalized per protein and expressed as percentage of untreated control.

Isolation of Mitochondria

Mitochondria from control and neurotoxin treated cells were isolated as described [10]. The crude mitochondrial fraction was suspended in isolation buffer and stored as aliquots at – 80 °C. Total protein in the mitochondrial preparation was estimated by Bradford method [14].

Mitochondrial Complex I Assay

CI enzyme activity was assayed in untreated and neurotoxin treated cells as described [10]. The rotenone-sensitive specific activity was calculated and expressed as percentage of untreated control.

Total Proteomics

Preparation of Cell Extracts

Control and treated N27 cells were sonicated in 1 × PBS with 1 × protease inhibitor cocktail (Sigma-Aldrich) using a probe sonicator for 10 s × 6 cycles (45% amplitude) on ice. The sonicate was centrifuged (10,000 g for 10 min at 4 °C) and the soluble extract corresponding to the supernatant was subjected to protein estimation by Bradford method [14]. During standardization and pilot experiments, we noted that other protocols had limitations including inconsistent protein yield in different replicates and problems with the extent of solubility. Hence this protocol was chosen for preparation of soluble extracts for proteomics experiments. Considering this, the protein profile might not represent the global proteome of the N27 dopaminergic cells.

Sample Preparation and TMT Labelling

Total cellular extracts (with equal protein as determined in the previous section) from untreated control (Group 1), Rot treated (LD_{25}-Group 2 and LD_{50}-Group 3), Pq treated (LD_{25}-Group 4 and LD_{50}-Group 5) MPP^+ treated (LD_{25}-Group 6 and LD_{50}-Group 7) were suspended in 2% SDS lysis buffer. The lysate was sonicated on ice and heated at 90 °C for 5 min followed by centrifugation (12,000 rpm for 15 min). Equal amount of protein (250 µg) from each sample was reduced using 5 mM of DTT at 60 °C for 60 min, alkylated with 20 mM iodoacetamide for 20 min at room temperature (RT) in dark, precipitated with chilled acetone at − 20 °C overnight and centrifuged (12,000 rpm at 4 °C for 15 min). The pellets were dissolved in 50 mM Triethyl ammonium bicarbonate (TEABC) buffer (pH 8.5) and then digested with sequencing grade modified trypsin (Promega) at 37 °C for 16 h and dried in a vacuum concentrator. Digested peptides were suspended in 100 µl 50 mM TEABC (pH 8.5) and labelled with TMT reagent as per the manufacturer's protocol. The samples from different groups were labelled as follows: 126 (control), 127N (Rot-LD_{25}), 128N (Rot-LD_{50}), 128C (Pq-LD_{25}) and 129N (Pq-LD_{50}), 129C (MPP^+-LD_{25}) and 130N (MPP^+-LD_{50}). The pooled sample was dried and fractionated into twelve fractions using basic pH reversed-phase liquid chromatography (bRPLC) as described [15]. Samples were reconstituted in 1 ml bRPLC solvent A (10 mM TEABC, pH 9.5). Increasing gradient of 7–100% solvent B (10 mM TEABC in 95% acetonitrile, pH 9.5) was employed to fractionate peptides using XBridge C_{18}, 5 µm, 250 × 4.6 mm column (Waters corporation, Milford, MA) with a flow rate of 500 µl/min for 120 min on an Agilent 1200 series HPLC system. The eluting peptides were collected in a 96 well plate and concentrated into 12 fractions. Each fraction was concentrated under vacuum and desalted using C_{18} stage tip clean up [7] followed by liquid chromatography-tandem mass spectrometry (LC–MS/MS).

LC–MS/MS

The peptides were analysed on an Orbitrap Fusion Tribrid mass spectrometer (Thermo Scientific, Bremen, Germany) interfaced with Easy-nLC 1000 nanoflow LC system (Thermo Scientific, Bremen, Germany). Vacuum dried peptide digests were reconstituted in 0.1% FA and loaded onto a 2 cm long pre-column (75 µm × 2 cm; nano Viper; C18; 3 µm particle and 100 Å pore size) (Thermo scientific Acclaim PepMap 100) using solvent A [0.1% formic acid (FA)] at a flow rate of 3 µl/min. Peptides were then resolved on analytical column (2 µm, 75 µm × 50 cm, 100 Å pore size) (Thermo scientific PepMap™ RSLC C18) using a linear gradient of 5% to 30% of solvent B [0.1% FA in 95% Acetonitrile (ACN)] over 100 min and flow rate of 300 nl/min. The total run time was set to 120 min. The MS was operated in a data-dependent acquisition mode. A precursor survey full scan MS (from m/z 350–1600) was acquired in the Orbitrap at a resolution of 120,000 at 200 m/z. The automatic gain control (AGC) target for MS1 was set as 4 X 10^5 and ion filling time set as 50 ms. The most intense ions with charge state ≥ 2 was isolated and fragmented using higher-energy collision-trap dissociation (HCD) fragmentation with 34% normalized collision energy and detected at a mass resolution of 50,000 at 200 m/z. The AGC target for MS/MS was set as 1 × 10^5 and ion filling time set as 100 ms. Isolation width was used as 1.6 m/z.

Data Analysis

Mass spectrometry derived raw data were searched against *Rattus norvegicus* database from UniProt (UP000002494-May 30th, 2021) along with known MS contaminants using SEQUEST search engine nodes on Proteome Discoverer 2.2 platform [7]. Trypsin was selected as the proteolytic enzyme and two missed cleavages were allowed during the search. Precursor and fragment ion mass tolerance were set to 10 ppm and 0.05 Da respectively. Carbamidomethylation of cysteine, TMT labelling at peptide N-terminus and lysine side chain were selected as static modification and oxidation of methionine was set as a dynamic modification. The data were filtered at 1% protein level false discovery rate (FDR). The reporter ion quantifier node was used to estimate relative quantitation of TMT channels from MS2 scans and normalization option was enabled. For any protein to be considered as significantly dysregulated, fold change above 1.5 as upregulated and below 0.6 as downregulated and p-value < 0.05 were considered. Since the number of differentially expressed proteins were very few, we performed manual analysis, where we identified the functions of each gene using Uniprot followed by literature survey and categorization.

Complex I (CI) Proteomics

Isolation of CI

CI was isolated using immunocapture method from N27 mitochondria using a commercial kit (Abcam) as per the manufacturer's protocol. Briefly, mitochondria (1 mg) were solubilized in ice-cold 1X PBS containing 1% N -dodecyl β-D-maltoside (DDM) for 30 min on ice and centrifuged (20,000 g for 30 min, 4 °C) [16]. The supernatant was incubated with agarose beads irreversibly cross-linked to CI-specific monoclonal antibody provided as part of the CI immunocapture kit (Abcam) overnight at 4 °C on a rocker. The beads were washed 5 times with 1 × PBS and the bound complex was eluted with 0.1 M glycine–HCl buffer, pH 2.5 supplemented with 0.05% DDM. These eluates were processed for in-solution tryptic digestion.

In-solution Tryptic Digestion

The eluates from CI immunocapture experiments were reduced with 10 mM DTT at 60 °C for 60 min, followed by alkylation with 20 mM Iodoacetamide (IAA) for 30 min at RT in dark. Alkylated proteins were precipitated by adding five volumes of chilled acetone and centrifuged at 12,000 rpm, 4 °C for 15 min. The pellets were dissolved in 40 mM ammonium bicarbonate (ABC) and then incubated with sequencing grade trypsin (Promega) (at 1:20, enzyme: protein) at 37 °C for 16 h. The reaction was stopped with 0.1% FA, purified on a C_{18} column and the peptide mixture was dried in a vacuum concentrator, followed by LC–MS/MS analysis.

LC–MS/MS

The peptides were analysed on an Orbitrap Fusion Tribrid mass spectrometer (Thermo Scientific, Bremen, Germany) interfaced with Easy-nLC 1000 nanoflow liquid chromatography system (Thermo Scientific, Bremen, Germany). Vacuum dried peptide digests were reconstituted in 0.1% FA and loaded onto a 2 cm long pre-column 75 µm × 2 cm, nano Viper, C_{18}, 3 µ particle and 100 Å pore size (Thermo scientific Acclaim PepMap 100) and analytical column 2 µm, 75 µm × 50 cm, 75 µm × 50 cm, 100 Å pore size (Thermo scientific PepMap™ RSLC C18) using a linear gradient of 5% to 30% of solvent B (0.1% FA in 95% ACN) over 100 min and flow rate of 300 nl/min. The total run time was set to 120 min. The MS was operated in a data-dependent acquisition mode. A precursor survey full scan MS (from m/z 350–1600) was acquired in the Orbitrap at a resolution of 120,000 at 200 m/z. The AGC target for MS1 was set as 4 X 10^5 and ion filling time set 50 ms. The most intense ions with charge state ≥ 2 was isolated and fragmented using HCD fragmentation with 34% normalized collision energy and detected at a mass resolution of 30,000 at 200 m/z. The AGC target for MS/MS was set as 1×10^5 and ion filling time set 100 ms and isolation width was used at 1.6 m/z.

Data Analysis

The acquired MS/MS data were processed through Proteome Discoverer platform (version 2.2 Thermo Scientific) using SEQUEST search algorithm against *Rattus norvegicus* protein database from UNIPROT (UP000002494- May 30th 2021) containing protein entries along with common MS contaminants. Trypsin allowing a maximum of two missed cleavages were selected as the proteolytic enzyme and oxidation of methionine and carbamidomethyl cysteine were set as dynamic modifications. For MS data, monoisotopic peptide mass tolerance was set to 10 ppm and MS/MS tolerance to 0.5 Da.

Based on the PTMs that were detected in the preliminary analysis without enrichment, the search parameters for the SEQUEST search algorithm focused on oxidation and dioxidation (W, C), trioxidation (C), cysteinylation (C), acetylation (N-terminal of protein and K), nitration (Y), methylation, Dimethylation and trimethylation (K, R), and phosphorylation (S, T, Y) as dynamic modifications and carbamidomethylation (C) as a static modification. While searching for Cysteine PTMs, carbamidomethylation was set as dynamic modification. The data were filtered at 1% level

FDR at peptide spectrum matches (PSMs). The confirmation of all PTMs was carried out based on manual analysis of MS data.

Oxyblot

Protein carbonyls in the protein extracts of the neurotoxic models were quantitated either by oxyblot method [17] or Biotin hydrazide method [18]. In oxyblot, the total cell extracts were derivatized by 2,4-dinitrophenylhydrazine (DNPH) followed by dot blot using anti-DNP antibody. In the biotin hydrazide method, total and mitochondrial extracts were derivatized with biotin hydrazide followed by western blot with anti-biotin antibody. The western signal was developed by enhanced chemiluminescence and visualized in a gel documentation system (Biorad). The images were quantified using Image J software [19] and normalized to their respective loading controls [β-Actin (1:3000) for total cellular protein and VDAC1 (1:3000) for mitochondrial protein] and expressed as percentage of untreated control.

Homology Modeling

The protein sequence of CI subunits was obtained from the Uniprot database (www.uniprot.org). Homology modeling was carried out to generate rat CI, using Discovery studio 3.5 with the mouse CI template (98% sequence identity between rat and mouse CI subunits) available at Protein Data Bank (PDB) with ID 6G2J. The protein model thus obtained was subjected to energy minimization and processed by applying CHARMM force field [20]. The potential energy of the structure was calculated using energy protocol available in Accelrys Discovery Studio 3.5.

Molecular Dynamics Simulation (MDS)

Preparation of the System

Five mutually interacting peripheral arm subunits of CI (NDUFV1, NDUFV2, NDUFV3, NDUFS1 and NDUFS4) were considered as a sub-complex for structural analysis. Among these, W433 in NDUFV1 subunit was replaced with oxindolylalanine (oxy-Trp or 2-OH Trp) to generate the oxidized subunit. The unmodified and Trp433 oxidized subcomplexes were subjected to MDS. The MDS solvent system of the subcomplexes was built using Desmond 2019. The Optimized Potentials for Liquid Simulations (OPLS) force field was added to the system and simple extended point charge (SPC) water system, along with a cubic box, was used to model the solvent. 1.5 mM of NaCl ions were added to neutralize the systems in the water-filled box. The MDS was set up for 100 ns under normal NTP [constant number of particles (N), temperature 310 k (T) and pressure-1 bar (P)] conditions. The system was relaxed prior to the simulation.

Analysis of Trajectories

After the simulation, the resultant 100 ns trajectories of the subunits of the unmodified subcomplex were analysed for protein backbone parameters such as Root Mean Square Deviation (RMSD) and Cα for Root Mean Square Fluctuation (RMSF). Further, all the subunits of the subcomplex were assessed for Radius of Gyration (Rg) throughout the duration of the simulation. The RMSD and Rg values were calculated against the simulation time and expressed as the deviation of radius of the selected group of atoms, respectively, in Å. The RMSF values of the Cα were calculated over the range of residues of the subunits and expressed as summation throughout the simulation for each residue fluctuation and denoted in Å. The distance between FMN and iron–sulfur cluster Fe-S301, FMN and iron–sulfur cluster Fe-S502, Fe-S301 and Fe-S502, Fe-S502 and Fe-S803, Fe-S803 and Fe-S802, and Fe-S802 and iron-sulfur cluster Fe-S801 were calculated for the unmodified and oxidized form. The Desmond module was used for the calculation of parameters. Maestro and PyMOL (www.pymol.org) were used for the generation of high-resolution illustrations [7].

Statistical Analysis

Quantitative data represented by bar graphs were accumulated from at least three independent experiments and expressed as mean ± SD. All analyses were performed using Microsoft Excel. For data related to validation experiments, analysis of variance (ANOVA) was performed and p-value < 0.05 was considered as significant. For all the MS based data, statistical analysis was carried out on Proteome Discoverer 2.2, which has integrated database search and statistical algorithms. Statistically corrected MS data was then uploaded on to Perseus (1.6.15.0) (http://www.perseus-framework.org) to generate a cluster based heatmap using Euclidean distance method.

Results

Proteomic Analysis of the Neurotoxic Models of PD

Neurotoxic models using Rot, Pq and MPP^+ mimic PD pathology via selective inhibition of CI and mitochondrial dysfunction [21]. However, whether these three neurotoxins induce similar degenerative pathways in dopaminergic neurons and PTMs of CI are not compared.

To address the first objective, we carried out comparative proteomic analysis of Rot, Pq, and MPP^+ neuronal cell models of PD at LD_{25} (representing early events of neurodegeneration) and LD_{50} (representing the neurotoxic phase) of each toxin compared to untreated control. Characterization of the three models revealed dose-dependent neurotoxicity as shown by cell viability assay (Rot- 0–2000 nM with $LD_{25} = 250$ nM and $LD_{50} = 500$ nM; Pq- 0–200 µM with $LD_{25} = 50$ µM and $LD_{50} = 100$ µM; MPP^+- 0–2000 µM with $LD_{25} = 150$ µM and $LD_{50} = 250$ µM) (Supplementary figure S1A–C) consistent with previous reports [22]. Subsequent experiments at LD_{25} and LD_{50} (vs. controls) revealed increased LDH activity (Supplementary figure S1D–E), elevated ROS (Supplementary figure S2A–C), lowered total glutathione (Supplementary figure S2D–F), increased protein carbonyls (Supplementary figure S3, S4 and S5) and inhibition of CI activity (Supplementary figure S6) in all the three models, consistent with previous results [11] and corroborating PD-specific neurotoxic mechanisms. Although these experiments were carried out both at 24 h and 48 h timepoints, we noted that the 48 h data was more consistent compared to the 24 h data in terms of cytotoxicity and other parameters across the three toxins. Hence, 48 h treatment regimen was followed throughout the study and used to calculate LD_{25} and LD_{50}.

Total proteomic analyses of the untreated control (Group 1) and three neurotoxic models at LD_{25} and LD_{50} (Groups 2 to 7) were carried out and compared across different groups (Fig. 1A and B). We identified 6400 proteins across all the groups, of which 1046 were mitochondrial and 5354 were non-mitochondrial proteins. Identified proteins were further categorized as dysregulated if they had a fold change ratio ≥ 1.5 and ≤ 0.6 and a p-value of ≤ 0.05. Using the aforementioned criteria, 89 differentially expressed proteins (DEPs) including 32 up-regulated and 57 down-regulated proteins across all the three toxic models, were noted at LD_{25} and LD_{50}. We analyzed the proteomic data obtained at LD_{25} and LD_{50} to obtain a comprehensive view of the molecular mechanisms underlying the neurotoxicity in PD.

Toxin-wise analysis revealed 55 DEPs in the Rot model (including 29 down-regulated and 26 up-regulated proteins), 52 DEPs in the Pq model (35 down-regulated and 17 up-regulated proteins) and 45 DEPs in the MPP^+ model (31 down-regulated and 14 up-regulated proteins) (Table 1 and Fig. 1C). Comparison of the proteomics data revealed that many up-regulated (n = 10) and down-regulated (n = 14) proteins were common across the three toxic models (Fig. 1D and E; volcano plots are shown in Fig. 1F–K). Interestingly, MPP^+ model revealed relatively fewer number of unique DEPs compared to the other two models.

Functional classification of DEPs revealed the involvement of biological processes mainly including cell death pathways, nuclear processes, protein and lipid metabolism, structural changes, immune responses, mitochondrial process and others (Fig. 2 and Table 1), most of which were common across the three models. Prominent pathways that could potentially contribute to neurotoxicity included cell death pathways, structural changes and metabolic alterations. Cell death pathways were represented by autophagy and cell cycle proteins. Among these, the protein Sequestosome (Sqstm1), involved in autophagy was significantly upregulated across all the toxins. On the other hand, the cell cycle controlling protein asparagine synthetase [glutamine-hydrolyzing] (Asns) and Prothymosin alpha (Ptma) that negatively regulates apoptosis was significantly downregulated (Table 1). Structural changes included upregulation of cytoskeletal proteins (Vimentin and Caldesmon) and disruption of extracellular matrix. The toxic insult also elicited stress response as indicated by the overexpression of chaperones such as Heat shock protein Hspb1 and Alpha Crystalline (B chain) (Cryab). Metabolic processes contributing to neurotoxicity mainly included lowered antioxidant response (as indicated by downregulation of SOD2) and downregulation of mitochondrial proteins. Altered antioxidant response could correspond to upregulated glutathione peroxidase (that could probably contribute to elevated GSSG, an indicator of oxidative stress) and thioredoxin domain containing protein 1 (Tmx1), that regulates redox dynamics.

Lowered expression of mitochondrial proteins included downregulation of electron transport chain (ETC) and pyruvate dehydrogenase complex. Among the ETC proteins, subunits of CI (including NDUFS6, NDUFA10, NDUFS1, NDUFS5) were downregulated. Other downregulated ETC proteins included cytochrome C oxidase subunits. Other metabolic proteins altered included succinate ligase [GDP-forming] subunit beta, aldehyde dehydrogenase and dihydrolipoyl dehydrogenase, delta (3,5)-delta (2,4)-dienoyl-CoA isomerase, medium-chain acyl-CoA ligase ACSF2 acyl-coenzyme A dehydrogenase and high affinity cationic amino acid transporter 1 (Table 1). Overall, we propose that neurotoxin-mediated CI inhibition triggers structural and functional pathways leading to neurodegeneration in dopaminergic neurons.

Proteomic Analysis of PTMs in CI of Neurotoxic Models

Proteomics data revealed downregulation of CI subunits in all three models. Since these neurotoxins targeted CI and caused inhibition of enzyme activity (Supplementary figure S6), we investigated whether the complex displayed PTMs following neurotoxic insult. Towards this, CI was isolated from untreated control and the three neurotoxic models by immunoprecipitation method followed by proteomic analysis (Fig. 3A). The subunit composition of the isolated complex was characterized by MS. Accordingly, 43 out of the

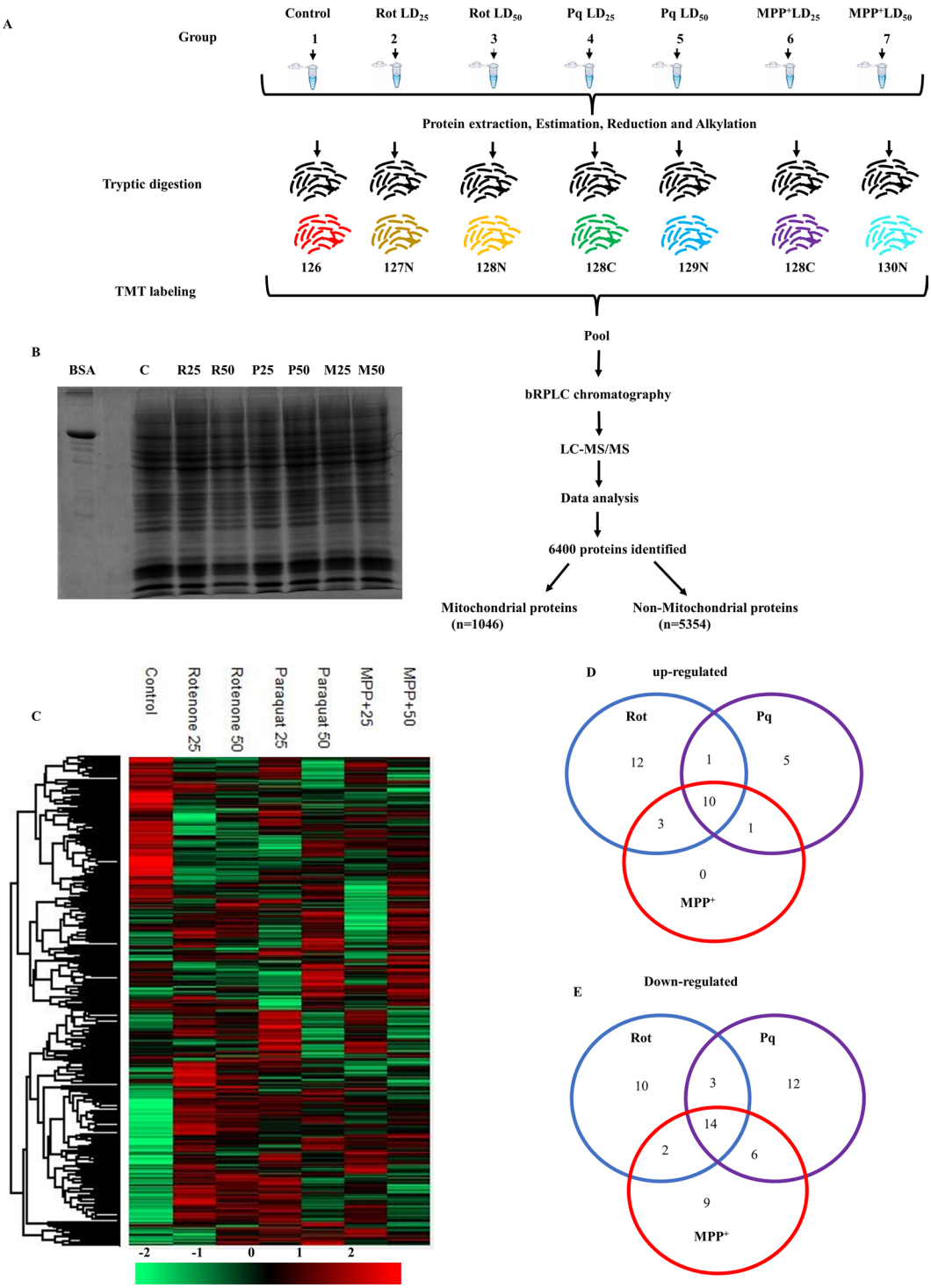

Fig. 1 Total Proteomic analysis in neurotoxic PD models. **A** Schematic representation of workflow of the Proteomics experiment. Total proteins (soluble extract) from control, Rot LD_{25} (R25), Rot LD_{50} (R50), Pq LD_{25} (P25), Pq LD_{50} (P50), MPP^+ LD_{25} (M25) and MPP^+ LD_{50} (M50) were subjected to tryptic digestion, followed by TMT labeling, fractionation, MS and data analysis. **B** SDS-PAGE profile of all the groups **(C)** Heat-map of differentially expressed proteins in different groups. The scale bar indicating the fold change in expression of individual proteins is also shown. Venn diagram shows the number of common and unique (**D**) up-regulated and (**E**) down-regulated proteins in Rot-, Pq- and MPP^+-treated cells. Volcano plots of the differentially expressed proteins in all the experimental groups are shown in **F–K**. Individual proteins ($p < 0.05$) corresponding to the down regulated (> 1.5 fold) and upregulated proteins (< 0.6 fold) (compared to the respective controls) are indicated in green and red respectively, while the proteins with unchanged expression are in black

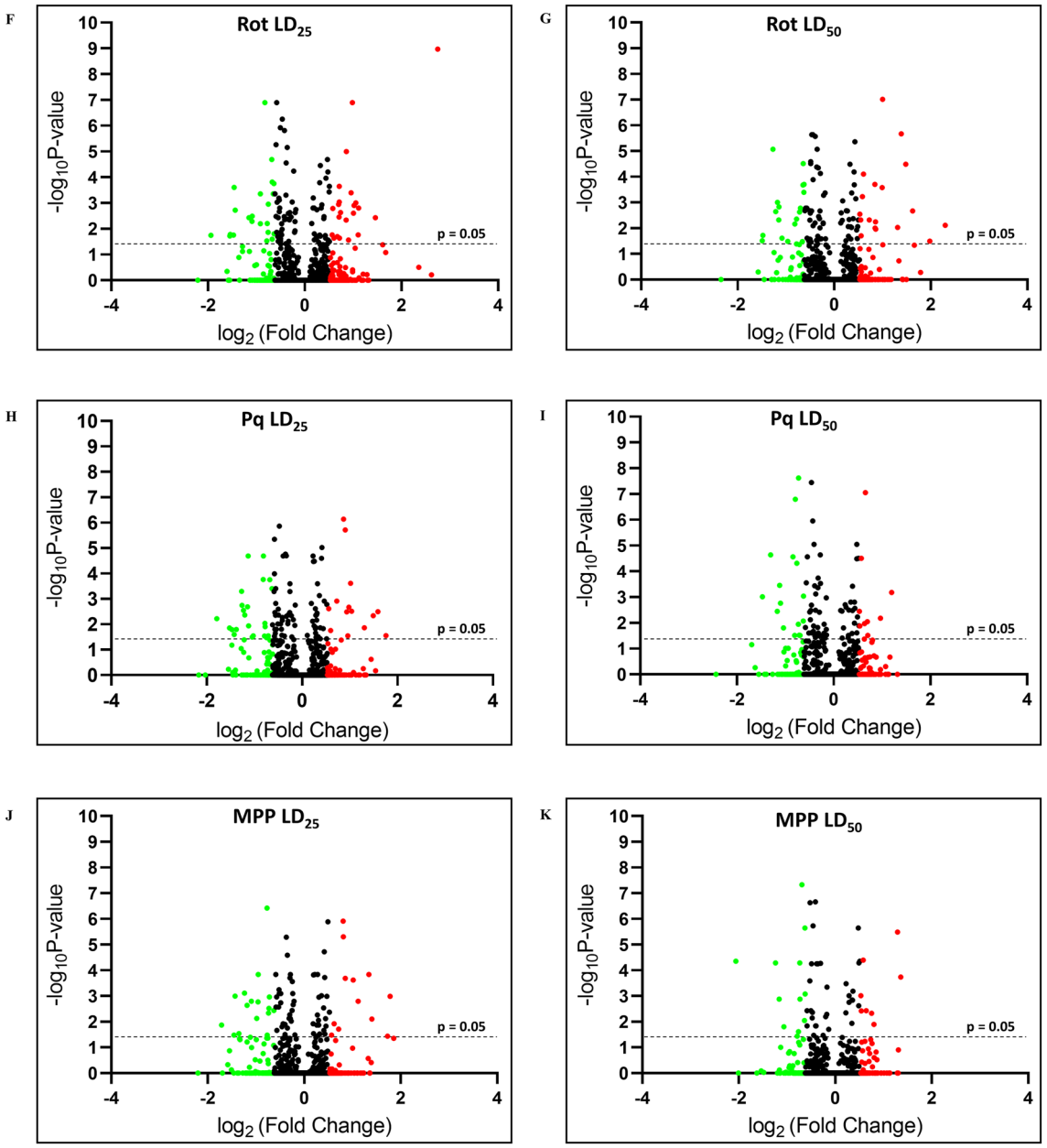

Fig. 1 (continued)

possible 44 subunits were identified in Rot (both LD_{25} and LD_{50}), Pq (LD_{25} and LD_{50}) and MPP^+ (LD_{50}) and 42 subunits in control and MPP^+ at LD_{25} (Table 2).

The LC–MS/MS data from the control and toxic models were mined for identification of 18 different PTMs (oxidative and non-oxidative) across the subunits of CI (Table 3). Data analysis revealed 66 PTMs in CI subunits, mainly including oxidative modifications (Trp oxidation and Cys oxidation) and limited non-oxidative modifications (Lys acetylation and Arg methylation). The toxic models revealed relatively higher number of PTMs compared to the untreated control. Supernumerary subunits of CI were targeted for PTMs to a greater extent compared to the core subunits, both in control and toxic models. Trp oxidation accounted for most of the oxidative PTMs (n = 62) including oxyindolylalanine (n = 29) and N-formylkynurenine (n = 33). On the other hand, limited Cys oxidation (n = 7) including trioxidation (Cys to Cys-sulfonic acid; n = 6) and cysteinylation (n = 1) was noted (Fig. 3B–D and Table 3). Representative m/z spectra showing Trp oxidation and Cys trioxidation in NDUFV1 are shown in Fig. 4.

Among the three toxins, Rot model showed higher number of PTMs followed by MPP^+ and Pq (Fig. 3E and Table 4) with Trp oxidation being the most predominant PTM.

Table 1 List of Differentially expressed genes across the Rot/Pq/MPP^+ models of PD. The accession ID, gene symbol and protein name along with the fold change in expression (vs. control) observed in the total proteomics experiment are provided. UC = unchanged

No	Accession ID	Gene	Proteins	Fold change (vs. control)					
				Rot		Pq		MPP^+	
				LD_{25}	LD_{50}	LD_{25}	LD_{50}	LD_{25}	LD_{50}
Cell death									
1	P49088	Asns	Asparagine synthetase [glutamine-hydrolyzing]	UC	UC	UC	0.59	UC	0.6
2	O08623	Sqstm1	Sequestosome-1	1.75	1.69	2.47	UC	2	UC
3	B2RZB5	Chmp2a	Charged multivesicular body protein 2A	1.81	1.5	UC	UC	UC	UC
4	Q8QZZ9	Cdkn2a	Tumor suppressor ARF	UC	UC	UC	1.56	1.54	UC
5	F1LW91	Numa1	Nuclear mitotic apparatus protein 1	UC	0.61	UC	UC	UC	UC
6	Q9EST6	Anp32b	Acidic leucine-rich nuclear phosphoprotein 32 family member B	UC	UC	UC	UC	0.61	UC
7	P06302	Ptma	Prothymosin alpha	0.64	UC	UC	UC	UC	UC
8	D3ZIE9	Aldh18a1	Delta-1-pyrroline-5-carboxylate synthase	UC	UC	UC	0.62	UC	UC
Nuclear processes									
9	Q5U2Q5	Rrm1	Ribonucleoside-diphosphate reductase	UC	UC	UC	1.75	UC	1.61
10	P52925	Hmgb2	High mobility group protein B2	0.47	0.6	UC	UC	0.58	UC
11	G3V8M1	Pold1	DNA polymerase	UC	UC	UC	UC	UC	0.6
12	D4A3K5	H1-1	Histone H1.1	0.36	0.33	0.35	UC	0.39	0.54
13	D3ZIX4	H1fx	H1.10 linker histone	0.5	0.46	0.37	UC	0.44	UC
14	D3ZXP3	H2afx	Histone H2A	0.62	0.64	UC	UC	UC	UC
15	D3ZJ08	Hist2h3c2	Histone H3	0.64	0.62	0.62	UC	0.37	0.64
16	B1WC28	H2afy2	Core histone macro-H2A	UC	UC	UC	0.6	UC	UC
17	P43138	Apex1	DNA-(apurinic or apyrimidinic site) endonuclease	0.64	UC	UC	UC	UC	UC
18	D3ZWF5	Eny2	Transcription and mRNA export factor ENY2	0.47	0.43	0.42	0.45	0.44	0.6
Protein and Lipid metabolism									
19	Q68SB1	Stau2	Double-stranded RNA-binding protein Staufen homolog 2	2.31	4.92	2.73	2.1	3.62	2.19
20	P38062	Metap2	Methionine aminopeptidase 2	UC	1.52	1.87	UC	1.75	UC
21	A0A0G2K7W6	RGD1562402	60S ribosomal protein L27a	0.58	0.57	UC	0.46	UC	UC
22	P50475	Aars1	Alanine—tRNA ligase	UC	UC	UC	UC	UC	0.59
23	A0A0H2UHG0	Yars	Tyrosine–tRNA ligase	UC	UC	UC	0.61	UC	0.62
24	D3ZWT2	Fitm2	Fat storage-inducing transmembrane protein 2	1.49	1.64	1.76	1.63	UC	UC
25	P17425	Hmgcs1	Hydroxymethylglutaryl-CoA synthase, cytoplasmic	2.01	1.8	UC	2.3	UC	2.56
26	P24268	Ctsd	Cathepsin D OS = Rattus norvegicus	0.59	UC	UC	UC	0.46	UC
27	P41350	Cav1	Caveolin-1 OS = Rattus norvegicus	0.59	0.42	0.46	UC	0.52	UC
28	G3V6S2	Aco1	Citrate hydro-lyase OS = Rattus norvegicus	UC	0.61	0.63	0.36	UC	0.24
29	D3Z955	Pgm2l1	Phosphoglucomutase 2-like 1	1.98	2	1.83	1.48	1.75	1.49
30	P04642	Ldha	L-lactate dehydrogenase A chain	UC	UC	UC	1.57	UC	UC
31	B2RYG2	Pck2	Phosphoenolpyruvate carboxykinase (GTP) (Fragment)	UC	UC	UC	0.63	UC	0.58

Table 1 (continued)

No	Accession ID	Gene	Proteins	Fold change (vs. control)					
				Rot		**Pq**		**MPP^+**	
				LD_{25}	**LD_{50}**	**LD_{25}**	**LD_{50}**	**LD_{25}**	**LD_{50}**
32	Q2YDV1	Dusp9	Dual specificity protein phosphatase	2.06	2.49	2.81	1.69	2.65	1.71
33	O08651	Phgdh	D-3-phosphoglycerate dehydrogenase	UC	UC	UC	0.65	UC	0.65
Structural changes									
34	G3V9E3	Cald1	Caldesmon 1, isoform CRA_b	1.94	1.99	2.02	1.62	2.02	1.69
35	G3V8C3	Vim	Vimentin OS = Rattus norvegicus	1.64	1.8	1.66	1.45	1.8	1.56
36	A0A0G2JWK7	Tagln	Transgelin OS = Rattus norvegicus	3.19	3.94	2.44	1.69	2.62	1.7
37	B5DFN4	Pfdn5	Prefoldin 5 (Predicted), isoform CRA_a	1.48	1.47	UC	UC	UC	UC
38	F1MAA7	Lamc1	Laminin subunit gamma 1	0.58	0.58	0.45	0.65	0.51	UC
39	D3ZFH5	Itih2	Inter-alpha-trypsin inhibitor heavy chain 2	0.56	UC	UC	0.58	0.59	0.65
40	A0A096P6L8	Fn1	Fibronectin	0.45	0.45	0.43	0.49	0.37	0.48
41	F1MAN8	Lama5	Laminin subunit alpha 5	0.53	0.45	0.42	0.57	0.42	0.59
42	B5DFC9	Nid2	Nidogen-2	0.41	0.36	0.36	0.58	0.4	0.52
Antioxidant and Immune response									
43	Q9Z1Z9	Pdlim7	PDZ and LIM domain protein 7	UC	1.46	UC	UC	UC	UC
44	F8WFK6	Gpx4	Glutathione peroxidase 4	1.67	1.65	1.51	UC	1.48	UC
45	P04041	Gpx1	Glutathione peroxidase 1	2.75	3.08	3.01	1.84	3.43	1.82
46	B2GVA1	Selenoo	Selenoprotein O OS	1.64	UC	UC	UC	UC	UC
47	P23928	Cryab	Alpha-crystallin B chain	1.63	UC	UC	UC	UC	UC
48	G3V913	Hspb1	Heat shock 27 kDa protein	1.81	1.81	1.52	1.49	1.57	UC
49	Q07258	Tgfb3	Transforming growth factor beta-3 proprotein	1.87	1.48	UC	1.5	UC	UC
50	Q5U2U5	Plin2	Perilipin	0.34	0.45	0.41	0.5	0.4	0.52
51	Q52KJ9	Tmx1	Thioredoxin domain containing protein 1	1.64	UC	1.47	UC	UC	UC
52	B2GV63	Chst14	Carbohydrate sulfotransferase	1.49	UC	UC	UC	UC	1.45
53	D3ZHV3	Mt1m	Metallothionein	0.59	UC	UC	UC	UC	UC
54	B2RYQ2	Ptpa	Serine/threonine-protein phosphatase 2A activator	UC	0.65	UC	0.56	UC	UC
55	P05942	S100a4	Protein S100-A4	2.08	UC	1.97	1.55	1.64	1.74
Mitochondrial process									
56	P07895	Sod2	Superoxide dismutase [Mn], mitochondrial	0.34	0.36	0.29	0.63	0.31	0.55
57	A0A0G2K3I1	Slc7a1	High affinity cationic amino acid transporter 1	0.53	0.58	UC	0.41	UC	0.42
58	D3ZCZ9	NDUFS6	NADH dehydrogenase [ubiquinone] iron-sulfur protein 6	0.61	0.61	0.38	0.49	0.47	0.46
59	A0A1W2Q6F8	Ndufa10l1	NADH dehydrogenase [ubiquinone] 1 alpha subcomplex subunit 10	UC	UC	0.49	0.57	0.59	0.56
60	Q66HF1	Ndufs1	NADH-ubiquinone oxidoreductase 75 kDa subunit	UC	UC	0.43	0.64	0.53	0.6
61	B5DEL8	Ndufs5	Complex I-15 kDa	UC	UC	0.46	0.59	0.56	0.58

Table 1 (continued)

No	Accession ID	Gene	Proteins	Fold change (vs. control)					
				Rot		**Pq**		**MPP$^+$**	
				LD_{25}	**LD_{50}**	**LD_{25}**	**LD_{50}**	**LD_{25}**	**LD_{50}**
62	P12075	Cox5b	Cytochrome c oxidase subunit 5B	UC	UC	0.63	UC	UC	UC
63	D3ZD09	Cox6b1	Cytochrome c oxidase subunit	UC	UC	0.63	UC	UC	UC
64	Q499N5	Acsf2	Medium-chain acyl-CoA ligase ACSF2	UC	0.64	0.57	UC	UC	UC
65	Q5M9H2	Acadvl	Acyl-Coenzyme A dehydrogenase, very long chain	UC	UC	0.6	UC	UC	UC
66	B2RYT0	Mrps21	Mitochondrial ribosomal protein S21	UC	UC	0.43	UC	UC	UC
67	G3V7J0	Aldh6a1	Aldehyde dehydrogenase family 6, subfamily A1, isoform CRA_b	UC	0.62	0.57	UC	0.65	UC
68	Q6P6R2	Dld	Dihydrolipoyl dehydrogenase	0.63	0.65	UC	UC	UC	UC
69	B1H270	Suclg2	Succinate–CoA ligase [GDP-forming] subunit beta	UC	0.61	UC	0.65	UC	0.64
70	Q62651	Ech1	Delta(3,5)-Delta(2,4)-dienoyl-CoA isomerase	UC	UC	0.61	UC	UC	UC
71	Q5PQQ1	Gtpbp3	tRNA modification GTPase	6.71	2.62	UC	UC	UC	2.45
Injury induced protein / toxic protein									
72	F1LQN3	Rtn4	Reticulon	1.52	UC	UC	UC	UC	UC
73	O54745	p65	p65 protein	1.83	3.16	2	1.57	2.51	1.79
74	F1M790	Ptgfrn	Prostaglandin F2 receptor negative regulator	2.16	1.81	2.06	1.95	2.17	1.7
Vesicles									
75	P24090	Ahsg	Alpha-2-HS-glycoprotein	0.26	0.44	0.52	0.31	0.34	0.45
76	B2RYP2	Litaf	LPS-induced TN factor	UC	UC	0.58	0.61	0.52	0.63
77	A0A0G2K0T2	Cd63	Tetraspanin OS = Rattus norvegicus	0.37	0.47	0.48	0.58	0.5	UC
Others									
78	A1A5L1	Blmh	Bleomycin hydrolase	0.63	0.63	UC	0.64	UC	UC
79	B2RZ20	Ssna1	SS nuclear autoantigen 1	UC	UC	UC	UC	0.6	UC
80	Q5XI04	Stom	RCG45489, isoform CRA_a	UC	UC	UC	UC	0.59	UC
81	B2GV63	Chst14	Carbohydrate sulfotransferase	1.49	UC	UC	UC	UC	1.45
82	M0RBK9	Pnkd	PNKD metallo-beta-lactamase domain-containing	2.15	2.01	UC	1.78	UC	1.75
83	Q9WTT7	Bzw2	Basic leucine zipper and W2 domain-containing protein 2	UC	UC	0.58	UC	0.59	UC
84	Q78EG7	Ptp4a1	Protein tyrosine phosphatase type IVA 1	0.36	0.44	0.58	0.47	0.47	0.45
85	A0A0H2UH90	Vwa5a	von Willebrand factor A domain-containing protein 5A	0.56	0.51	0.58	UC	0.56	UC
86	G3V645	Oasl	2'-5'-oligoadenylate synthase-like protein 1	1.62	UC	UC	UC	UC	UC
87	B0BMW4	Gnas	GNAS complex locus	0.64	UC	UC	UC	UC	UC
88	Q99NH3	Rab3il1	Guanine nucleotide exchange factor for Rab-3A	UC	UC	1.94	UC	UC	UC
89	M0RCA0	Foxc1	Forkhead box C1	UC	UC	UC	UC	0.6	UC

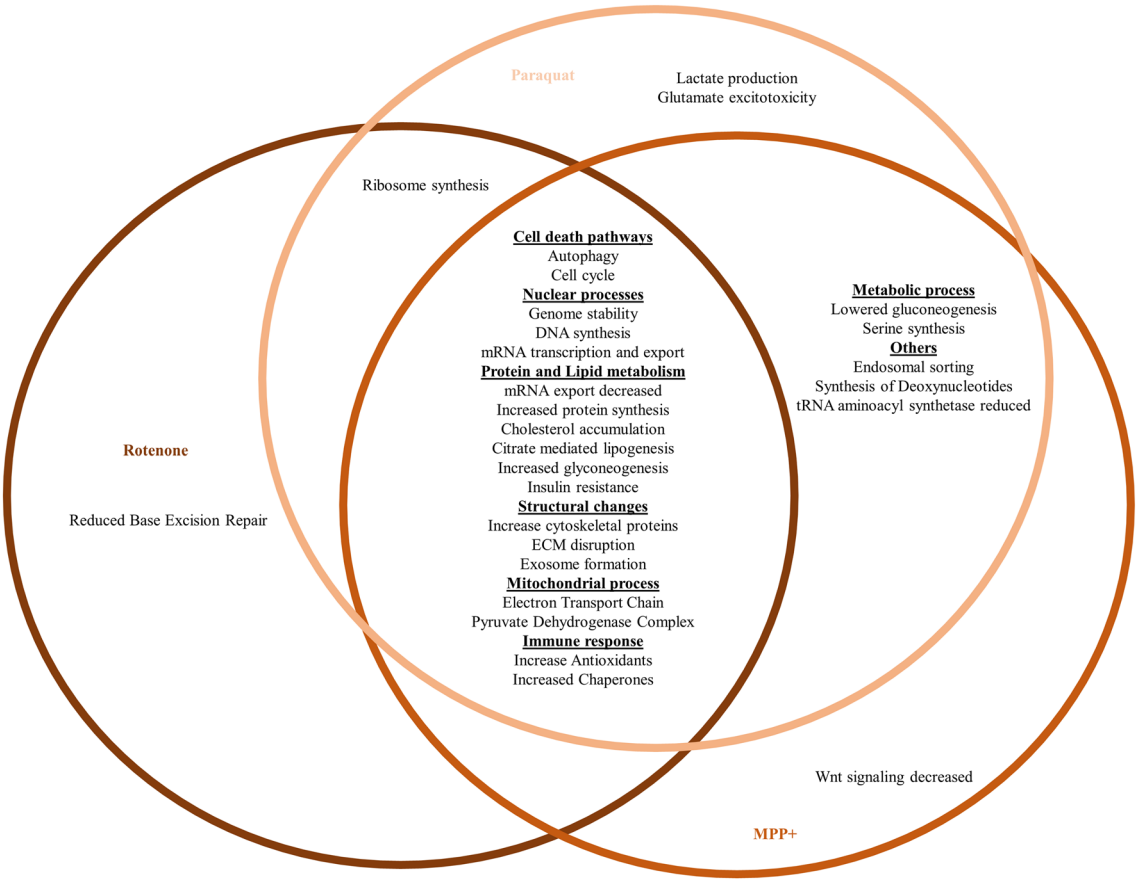

Fig. 2 Schematic representation of cellular events in neurotoxic PD models. Summary of the trend of different biological processes that are altered at the total proteome level in different neurotoxic models (Rot, Pq and MPP^+). Each circle represents each neurotoxin and the common process for all 3 neurotoxins are listed in the middle

Analysis of the distribution of the PTMs across different subunits of CI revealed that the peripheral arm had relatively higher number of PTMs compared to the membrane arm. Among the subunits, NDUFV1 showed the maximum number of PTMs followed by NDUFA9 and NDUFS1 (Fig. 3F and Fig. 5 and Table 4). Table 5 lists the 15 PTMs from our study that were previously identified by other groups.

Apart from the identification of PTMs, it is pertinent to understand the effect of these on the structure–function relationship of CI. Towards this, we carried out structural analysis of CI subunits and compared the local structural changes between the unmodified and modified sub-complexes.

Molecular Modelling and MDS of CI Subunits

Our MS data revealed that Trp oxidation is the most predominant PTM in the neurotoxic models, potentially contributing to the altered structure–function relationship of the complex. Since the data were generated using a rat neuronal cell line (N27), we chose to generate a 3D model of rat CI using the available mouse complex structure (PDB ID: 6G2J) as template, using standard methods [23]. The obtained protein model was energy minimized to determine the proper molecular arrangement in space and considered an unmodified CI (Fig. 6A).

Next, we selected five peripheral arm subunits (NDUFV1, NDUFV2, NDUFV3, NDUFS1 and NDUFS4) that interact with each other and harbor the critical sites including the FMN binding site and Fe-S clusters. This sub-complex was chosen for structural analysis by MDS experiment to assess the effects of Trp oxidation (Fig. 6B i and ii). After careful analysis of Trp oxidation events in these subunits, Trp433 in NDUFV1 was chosen for further study. Since this residue was proximal to the NADH, FMN and Fe-S site and was oxidized (Trp to oxyindolylalanine) in the neurotoxic model, we chose to assess the structural perturbations caused by this PTM. Accordingly, the sub-complex (with five subunits) with Trp433 in NDUFV1 was replaced with oxyindolylalanine (and all the other Trp residues across the five subunits present in the unmodified state) was considered as "modified" structure and compared with the unmodified sub-complex.

A

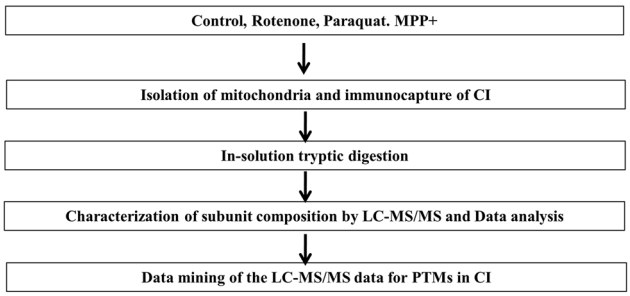

B

Types of PTMs	W	C	K	R
Oxidation	29	-	-	-
Dioxidation	33	-	-	-
Trioxidation	-	6	-	-
Cysteinylation	-	1	-	-
Acetylation	-	-	1	-
Dimethylation	-	-	-	1
Total	**62**	**7**	**1**	**1**

C

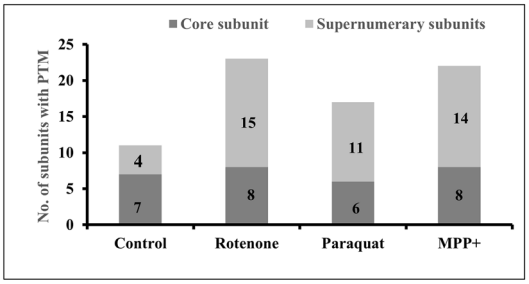

D

Group	Oxidation	Dioxidation	Trioxidation	Dimethylation	Acetylation	Cysteinylation	Total
Control	3	10	1	1	-	-	**15**
Rotenone	27	32	5	1	-	1	**66**
Paraquat	11	19	1	1	-	-	**32**
MPP+	17	22	1	1	1	-	**42**

E

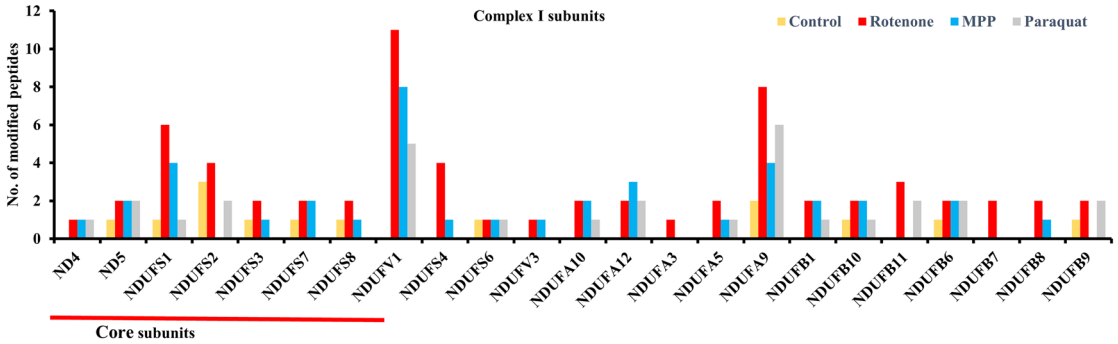

Fig. 3 Immunocapture of mitochondrial Complex I (CI) and PTM characterization. **A** Experimental workflow. Total mitochondria were isolated from Control, Rot, Pq and MPP$^+$. CI was immunocaptured individually from each group and subjected to in-solution tryptic digestion and LC–MS/MS followed by subunit characterization. The MS data was mined to identify PTMs in different subunits of CI. **B** The table shows the types and number of PTMs at Trp (W), Cys (C), Lys (K) and Arg (R) residues across different control and toxic models **(C)** Graph shows the number of core and supernumerary subunits with PTMs. **D** The type and number of PTMs across control and toxic models. **E** The number of modified peptides in CI in control and toxic models. The subunits underlined in red are the core subunits of CI

MDS analysis (0–100 ns or 0–1000 frames) of the unmodified and modified sub-complexes were carried out, followed by the calculation of RMSD, RMSF and Rg for all the subunits (Fig. 7). The RMSD values of the modified subunits showed significant variation in subunits NDUFV1 and the interacting subunit NDUFS4. The backbone of the modified NDUFV1and NDUFS4 subunit displayed altered RMSD from 160 (16 ns) and 60 (6 ns) frames respectively.

Table 2 Summary of the MS characterization of CI subunits

No.	Accession	Subunit	# AAs and MW (kDa)	Description	Control	Rotenone		Paraquat		MPP^+	
						LD_{25}	LD_{50}	LD_{25}	LD_{50}	LD_{25}	LD_{50}
1	B4F7B9	Ndufa1	86(9.772)	NADH dehydrogenase [ubiquinone] 1 alpha subcomplex subunit 1-MWFE (Fragment)	+	+	+	+	+	+	+
2	D3ZS58	Ndufa2	97(10.838)	NADH dehydrogenase [ubiquinone] 1 alpha subcomplex subunit 2	+	+	+	+	+	+	+
3	A0A0G2KAA3	Ndufa3	91(10.163)	NADH dehydrogenase [ubiquinone] 1 alpha subcomplex subunit 3-B9	+	+	+	+	+	+	+
4	Q63362	Ndufa5	116(13.403)	NADH dehydrogenase [ubiquinone] 1 alpha subcomplex subunit 5	+	+	+	+	+	+	+
5	D4A3V2	Ndufa6	130(15.214)	NADH dehydrogenase [ubiquinone] 1 alpha subcomplex subunit 6	+	+	+	+	+	+	+
6	A9UMV9	Ndufa7	112(12.493)	NADH dehydrogenase [ubiquinone] 1 alpha subcomplex subunit 7-B14.5a	+	+	+	+	+	+	+
7	F7EXQ7	Ndufa8	190 22.108)	NADH dehydrogenase [ubiquinone] 1 alpha subcomplex subunit 8-19kD	+	+	+	+	+	+	+
8	Q5BK63	Ndufa9	377(42.532)	NADH dehydrogenase [ubiquinone] 1 alpha subcomplex subunit 9	+	+	+	+	+	+	+
9	Q561S0	Ndufa10	355(40.468)	NADH dehydrogenase [ubiquinone] 1 alpha subcomplex subunit 10	+	+	+	+	+	+	+
10	Q80W89	Ndufa11	141(14.844)	NADH dehydrogenase [ubiquinone] 1 alpha subcomplex subunit 11	+	+	+	+	+	+	+
11	F1LXA0	Ndufa12	145(17.167)	NADH dehydrogenase [ubiquinone] 1 alpha subcomplex subunit 12	+	+	+	+	+	+	+
12	D3ZE15	Ndufa13	144(16.766)	NADH dehydrogenase [ubiquinone] 1 alpha subcomplex subunit 13	+	+	+	+	+	+	+
13	D3ZF13	Ndufab1	156(17.503)	Acyl carrier protein	+	+	+	+	+	+	+
14	P0DN35	Ndufb1	57(6.994)	NADH dehydrogenase [ubiquinone] 1 beta subcomplex subunit 1	+	+	+	+	+	+	+
15	B2RYU0	Ndufb2	105(11.835)	NADH dehydrogenase [ubiquinone] 1 beta subcomplex subunit 2-AGGG	+	+	+	+	+	+	+
16	D4A4P3	Ndufb3	99(11.26)	NADH dehydrogenase [ubiquinone] 1 beta subcomplex subunit 3-B12	+	+	+	+	+	+	+
17	F1LPG5	Ndufb4	129(15.055)	NADH dehydrogenase [ubiquinone] 1 beta subcomplex subunit 4-B15	+	+	+	+	+	+	+
18	D4A565	Ndufb5	189(21.65)	NADH dehydrogenase [ubiquinone] 1 beta subcomplex subunit 5-SGDH	+	+	+	+	+	+	+
19	D3ZZ21	Ndufb6	128(15.628)	NADH dehydrogenase [ubiquinone] 1 beta subcomplex subunit 6-B17	+	+	+	+	+	+	+
20	D3ZLT1	Ndufb7	137(16.557)	NADH dehydrogenase [ubiquinone] 1 beta subcomplex subunit 7-B18	+	+	+	+	+	+	+

Table 2 (continued)

No.	Accession	Subunit	# AAs and MW (kDa)	Description	Control	Rotenone		Paraquat		MPP^+	
						LD_{25}	LD_{50}	LD_{25}	LD_{50}	LD_{25}	LD_{50}
21	B2RYS8	Ndufb8	186(21.944)	NADH dehydrogenase [ubiquinone] 1 beta subcomplex subunit 8	+	+	+	+	+	+	+
22	B2RYW3	Ndufb9	179(21.878)	NADH dehydrogenase [ubiquinone] 1 beta subcomplex subunit 9-B22	+	+	+	+	+	+	+
23	D4A0T0	Ndufb10	176(20.845)	NADH dehydrogenase [ubiquinone] 1 beta subcomplex subunit 10-PDSW	+	+	+	+	+	+	+
24	D4A7L4	Ndufb11	151(17.623)	NADH dehydrogenase [ubiquinone] 1 beta subcomplex subunit 11-ESSS	+	+	+	+	+	+	+
25	D3ZS75	Ndufc1	76(8.781)	NADH dehydrogenase [ubiquinone] 1 subunit C1-KFYI	-	+	+	+	+	-	+
26	Q5PQZ9	Ndufc2	120(14.349)	NADH dehydrogenase [ubiquinone] 1 subunit C2	+	+	+	+	+	+	+
27	Q66HF1	Ndufs1	727(79.362)	NADH-ubiquinone oxidoreductase 75 kDa subunit, mitochondrial	+	+	+	+	+	+	+
28	Q641Y2	Ndufs2	463(52.528)	NADH dehydrogenase [ubiquinone] iron-sulfur protein 2	+	+	+	+	+	+	+
29	D3ZG43	Ndufs3	264(30.208)	NADH dehydrogenase [ubiquinone] iron-sulfur protein 3-30kD	+	+	+	+	+	+	+
30	Q5XIF3	Ndufs4	175(19.728)	NADH dehydrogenase [ubiquinone] iron-sulfur protein 4	+	+	+	+	+	+	+
31	B5DEL8	Ndufs5	106(12.691)	NADH dehydrogenase [ubiquinone] iron-sulfur protein 5–15 kDa	+	+	+	+	+	+	+
32	D3ZCZ9	Ndufs6	116(13.032)	NADH dehydrogenase [ubiquinone] iron-sulfur protein 6	+	+	+	+	+	+	+
33	Q5RJN0	Ndufs7	218(23.929)	NADH dehydrogenase [ubiquinone] iron-sulfur protein 7-20kD	+	+	+	+	+	+	+
34	B0BNE6	Ndufs8	212(23.955)	NADH dehydrogenase [ubiquinone] iron-sulfur protein 8-23kD	+	+	+	+	+	+	+
35	Q5XIH3	Ndufv1	464(50.699)	NADH dehydrogenase [ubiquinone] flavoprotein 1	+	+	+	+	+	+	+
36	P19234	Ndufv2	248(27.361)	NADH dehydrogenase [ubiquinone] flavoprotein 2	+	+	+	+	+	+	+
37a	G3V644	Ndufv3	458(49.27)	NADH dehydrogenase [ubiquinone] flavoprotein 2-9kD	+	+	+	+	+	+	+
37b	Q6PCU8	Ndufv3	108(11.934)	NADH dehydrogenase [ubiquinone] flavoprotein 3	-	-	-	-	-	-	+
38	D2E6L7	ND1	318(36.038)	NADH-ubiquinone oxidoreductase chain 1	+	+	+	+	+	+	+
39	A0A0A1G491	ND2	345(38.517)	NADH-ubiquinone oxidoreductase chain 2	+	+	+	+	+	+	+
40	A0A0A1FZ38	ND3	115(13.062)	NADH-ubiquinone oxidoreductase chain 3	+	+	+	+	+	+	+
41	D2E6K0	ND4	459(51.798)	NADH-ubiquinone oxidoreductase chain 4	+	+	+	+	+	+	+
42	P05507	ND4L	98(10.651)	NADH-ubiquinone oxidoreductase chain 4L	+	+	+	+	+	+	+
43	A0A096XKT9	ND5	609(68.538)	NADH-ubiquinone oxidoreductase chain 5	+	+	+	+	+	+	+
44		ND6		NADH-ubiquinone oxidoreductase chain 6	-	-	-	-	-	-	-
No. of subunits identified in each condition					**42**	**43**	**43**	**43**	**43**	**42**	**43**

Accession number, subunit symbol, number of amino acids (AAs) and Molecular Weight (MW) and description of each subunit and its detection in different brain regions and muscle types along with the total number of subunits identified ('+' = detected; '- ' = not detected) are indicated

Table 3 List of Post Translational Modifications (PTMs) searched in the CI MS data. The type of PTM, targeted residues, mass difference (Δm) and the reaction are shown

No	PTMs	Targeted Residues	Δm (monoisotopic)	Reaction
Oxidative PTMs				
1	Glutamic semialdehyde	R	− 43.05	Arg to Glutamic semialdehyde
2	Oxidation	W, C	15.99	Trp to Oxyindolylalanine, Cys to Cys-sulfenic acid
3	Dioxidation	W, C	31.99	Trp to N-formylkynurenine, Cys to Cys-sulfinic acid
4	Trioxidation	C	47.98	Cys to Cys-sulfonic acid
5	Cysteinylation	C	119	Cystine disulfide
6	Hydroxykynurenine	W	19.99	Trp to Hydroxykynurenine
7	Kynurenine	W	3.99	Trp to Kynurenine
8	Oxolactone	W	13.98	Trp to Oxolactone
Non-Oxidative PTMs				
9	Acetylation	N-terminus, K, C	42.04	N-Acetyl protein, Lys to Acetyl-lys
10	Palmitoylation	N-terminus, K, C	238.23	N-Palmitoyl protein, Lys to N-Palmitoylated Lys, Cys to S-Palmitoyl Cys
11	Glutathionylation	C	305.07	Cys to S-Glutathionylated Cys
12	Nitrosylation	C	28.99	Cys to S-nitrosylated cys
13	Phosphorylation	S, T, Y	79.97	Ser to Phospho-ser, Thr to Phospho-thr, Tyr to Phospho-tyr
14	Nitration	Y	44.99	Tyr to 3-Nitro tyr
15	Sulfation	Y	79.96	Tyr to Sulfo tyr
16	Methylation	K, R	14.02	Lys to Methyl lys, Arg to methyl arg
17	Dimethylation	K, R	28.03	Lys to Dimethyl lys, Arg to Dimethyl arg
18	Trimethylation	K, R	42.05	Lysine to Trimethyl lys, Arg to Trimethyl arg

However, the other interacting subunits of NDUFV1 i.e., NDUFV2, NDUFV3 and NDUFS1 did not show significant structural changes following the oxidation of Trp433 (Fig. 7A–E). RMSF data showed significantly increased fluctuation in modified NDUFV1 and NDUFV3 whereas modified NDUFV2 and NDUFS1 showed decreased fluctuation compared to unmodified conditions (Fig. 7G). The changes noted in the RMSF data indicate local structural changes in individual subunits. However, the overall structure of the sub-complex was relatively unaltered as indicated by Rg analysis (Fig. 7F).

Since most of the subunits showed local conformational changes in selected regions, we investigated whether these could impinge on the distances between consecutive Fe-S clusters, thereby potentially altering the enzyme activity. We noted that the distance between Fe-S 301 (N1a) to Fe-S 502 (N3) (in NDUFV1) and Fe-S 802 (N4) to Fe-S 801 (N5) (both in NDUFS1) were decreased by ~2 Å (Fig. 8) in the entire simulation, indicating that oxidation of W433 alters the local confirmation in NDUFV1 and the neighbouring subunits indicating the long-distance conformational changes induced by a single W oxidation.

The local conformational changes in these subunits were further analysed by hydrogen bond analysis at the subunit level and the residue level. The number of hydrogen bonds between NDUFV1 and NDUFS1 and between NDUFV1 and NDUFS4 were significantly reduced in the modified structure, compared to unmodified conditions (Fig. 9C and D). However, the hydrogen bonding between NDUFV1 and NDUFV2 and between NDUFV1 and NDUFV3 were relatively unaltered throughout the simulation (Figs. 9A to D). Structural analysis at the residue level revealed significant increase in the distance between the sidechains of W433 and the neighbouring residues G437 in the modified structure (3.68 Å at 100 ns) compared to the unmodified structure (2.23 Å at 100 ns) thereby leading to loss of hydrogen bond between the two residues (Fig. 9I). Interestingly, the loss of this hydrogen bond converted the helical structure into a loop, thereby indicating alterations in the local secondary structure.

Discussion

Many neurotoxic PD models have been characterized but none of them recapitulate all the pathological features of the disease [21]. Models employing neurotoxins have focused on CI inhibition-mediated mitochondrial damage as the primary event of PD pathogenesis. Considering the varied response of neurotoxins that targets CI, we tried to identify common characteristics of neurodegeneration in PD using three neurotoxins that inhibit CI. The characterization of these models

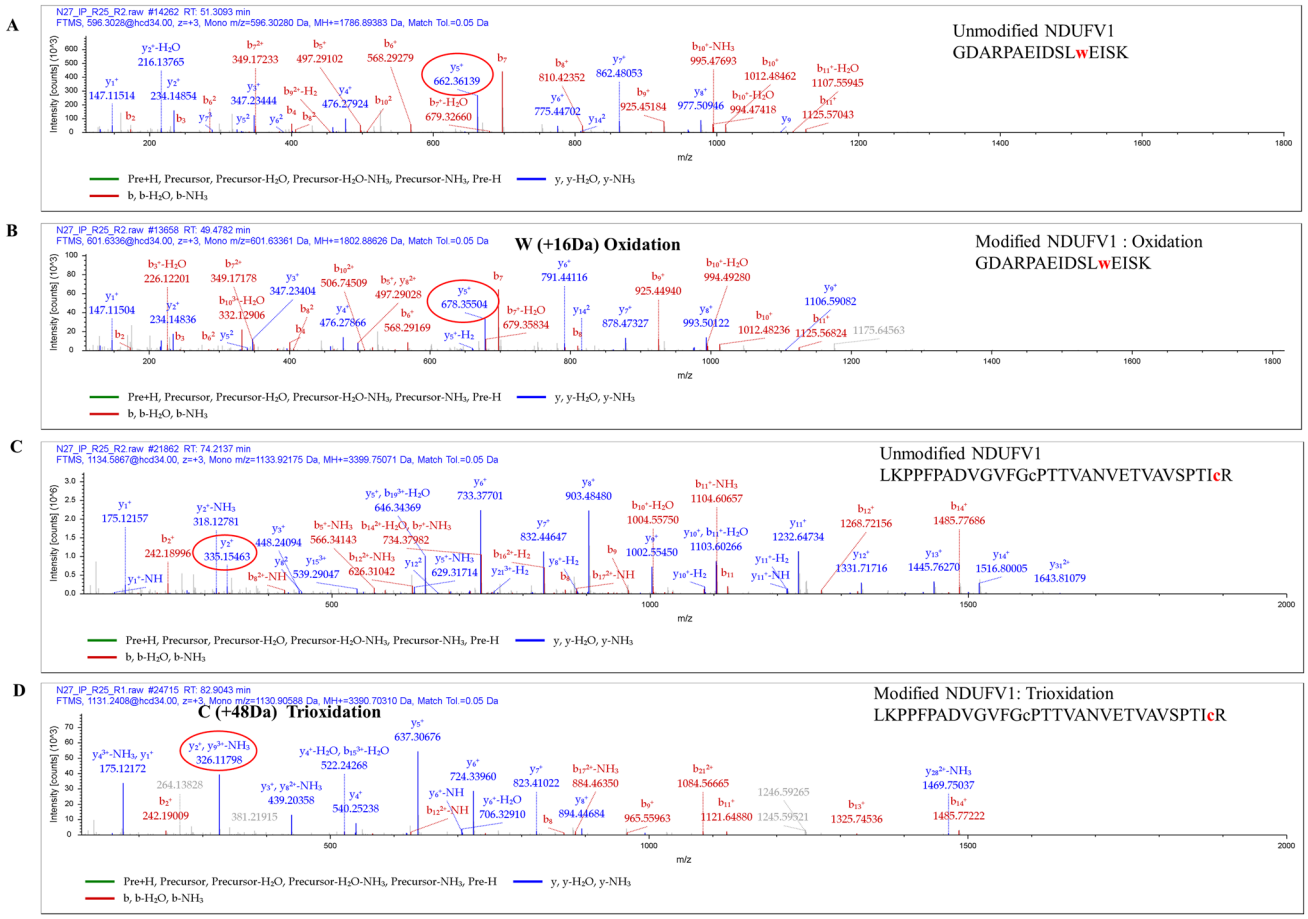

Fig. 4 Representative m/z spectra of Trp (W), Cys (C) PTMs in Complex I subunits. m/z spectra of unmodified and modified peptides in NDUFV1 subunit are shown. **A–B,** W oxidation spectra. **A**, m/z spectra of a peptide (sequence shown with the susceptible Trp (W) shown in red, lower case) showing unmodified Trp. **B**, m/z Spectra of the same peptide with oxidized Trp (Trp to Oxyindolylalanine) with mass increase of 16 Da (indicated as + 16 Da). **C–D,** C oxidation spectra. **C,** m/z spectra of the peptide (sequence shown with the susceptible C shown in red, lower case) with unmodified C. **D**, m/z Spectra of the peptide with C Trioxidation (Cys to Cys-sulfonic acid) with mass increase of 48 Da (indicated as + 48 Da)

will not only provide insights into CI damage and cell death but also assist in developing novel therapeutics.

Proteomic Changes in the Neurotoxic Models of PD

Previous "omics" studies in PD patients and models have identified degenerative pathways including mitochondrial dysfunction, impaired energy production, oxidative stress, proteasomal dysfunction, impaired cytoskeleton organization, or elevated inflammation [24–27]. Many genetic models of PD have revealed mitochondrial dysfunction and oxidative damage. Parkin-/- mice display altered expression of glycolytic, mitochondrial (subunits of TCA, OXPHOS and pyruvate dehydrogenase) and antioxidant proteins (peroxiredoxins) [28, 29]. Previous studies including ours [11, 30] linked mutant α-synuclein with impaired energy metabolism, mitochondrial dysfunction and oxidative stress [30]. Similarly, PINK1 deficiency induces proteomic changes linked to impaired glycolysis, mitochondrial respiration [31, 32] and oxidative stress [33].

Proteomics in the Rot model revealed altered expression of proteins implicated in mitochondrial, endoplasmic reticulum, autophagy, cytokinesis, cell cycle and cytoskeleton functions [34, 35]. Our previous microarray study in the MPP^+ model noted differential expression of mitochondrial, synaptic and autophagy genes linked with apoptosis, neuroinflammation, neurotransmission and cytoskeleton organization [36, 37]. MPTP models have revealed alterations in proteins of redox, mitochondrial [38] and protein deglycase (DJ-1) function [39].

Although gene and protein expression data are available for MPP^+ and Rot model, such studies in Pq model are limited. Further, comparative proteomic analysis across three neurotoxic models (Rot, Pq and MPP^+) is not reported so far. The current study noted 10 up-regulated and 14 down-regulated proteins common across three neurotoxic models

Table 4 List of PTMs identified in isolated CI. The accession number and symbol of the subunit, annotated peptide sequence [modified residues in lower case (bold)], amino acid (AA) position in the protein, specific PTM and the sample are shown (Rot LD_{25} = R25, Rot LD_{50} = R50, Pq LD_{25} = P25, Pq LD_{50} = P50, MPP^+ LD_{25} = M25 and MPP^+ LD_{50} = M50)

Accession	Subunit	Annotated Sequence	AA position in the protein (PTM in parenthesis)	Found in Sample
A0A0G2KAA3	NDUFA3	DNGNMPDVPSHPQEPLGP-SLEwLK	W22(Dioxidation)	R25
Q63362	NDUFA5	mLQWKPWEPLVEEPPANQwK	M1(Oxidation); W19(Dioxidation)	R25, P50
		TTGLVGLAVcDTPHER	C10(Trioxidation)	R25
Q5BK63	NDUFA9	LFGLSPFEPwTTK	W10(Oxidation)	R25, P25
		LFGLSPFEPwTTK	W10(Dioxidation)	Control, R25
		LMGDLGQLIFLEwDAR	W13(Dioxidation)	Control, R25, M25, P25, P50
		cDIYDTmHLR	C1(Trioxidation); M7(Oxidation)	R25
		FVYSwIGR	W5(Dioxidation)	R25, R50, P25
		FVYSwIGR	W5(Oxidation)	R25, M25, P25, P50
		LmGDLGQLIFLEwDAR	M2(Oxidation); W13(Oxidation)	R25, M25, P25, P50
		wLSSEIEETKPAK	W1(Oxidation)	R25, M25, P25, P50
Q561S0	NDUFA10	LQSwLYASR	W4(Dioxidation)	R25, R50, M25, P25, P50
		LQSwLYASR	W4(Oxidation)	R25, M25
F1LXA0	NDUFA12	QEwVPPSTPYK	W4(Oxidation)	R25, M25
		IQEwVPPSTPYK	W4(Dioxidation)	R50, M25
		wLHcMTDDPPTTKPLTAR	W1(Oxidation); C4(Carbamidomethyl)	M25, P25, P50
		NTFWDVDGSMVPPEwHR	W15(Dioxidation)	P50
D3ZF13	NDUFAB1	LYDkIDPEK	K4(Acetyl)	M50
P0DN35	NDUFB1	ELRPNEEVTwK	W10(Dioxidation)	R25, M25, M50, P25, P50
		ELRPNEEVTwK	W10(Oxidation)	R25, R50, M25, M50
D3ZZ21	NDUFB6	FwNNFLR	W2(Dioxidation)	Control, R25, R50, M25, P25, P50
		MwPLER	W2(Dioxidation)	R25, M25, P25
D3ZLT1	NDUFB7	DSFPNFVAcK	C9(Trioxidation)	R25
		YLwDASVEPDPEK	W3(Dioxidation)	R25
B2RYS8	NDUFB8	VDTSPTPVSwDVmcR	W10(Dioxidation); M13(Oxidation); C14(Carbamidomethyl)	R25, M25
		DPWYEwDHPDLR	W6(Oxidation)	R25
B2RYW3	NDUFB9	mESwDR	M1(Oxidation); W4(Dioxidation)	Control, R25, R50, M50, P25, P50
		HLESwcVHR	W5(Oxidation); C6(Carbamidomethyl)	R25, R50, P50
D4A0T0	NDUFB10	AYDLVVDwPVTLVR	W8(Dioxidation)	Control, R25, R50, M25, M50
		AYDLVVDwPVTLVR	W8(Oxidation)	R25, R50, M25, P50
D4A7L4	NDUFB11	NPDFHGYDSDPVVDVwNmR	W16(Dioxidation); M18(Oxidation)	R25, P50
		NPDFHGYDSDPVVDVwNmR	W16(Oxidation); M18(Oxidation)	R25
		mQEwAR	M1(Oxidation); W4(Dioxidation)	R50, M50, P25, P50
Q66HF1	NDUFS1	MHEDINEEwISDK	W9(Dioxidation)	Control, R25, R50, P25, P50
		MHEDINEEwISDK	W9(Oxidation)	R25, M25
		GLLTYTSwEDALSR	W8(Dioxidation)	R25, M25
		GLLTYTSwEDALSR	W8(Oxidation)	R25, R50
		VASGAAAEwK	W9(Dioxidation)	R25, R50, M50
		AVTEGAQAVEEPSIc	C15(Cysteinyl)	R50
		VASGAAAEwK	W9(Oxidation)	R50, M50

Table 4 (continued)

Accession	Subunit	Annotated Sequence	AA position in the protein (PTM in parenthesis)	Found in Sample
Q641Y2	NDUFS2	GSGIQwDLR	W6(Dioxidation)	Control, R25, R50, P25, P50
		GSGIQwDLR	W6(Oxidation)	Control, R25, R50
		KcDPHIGLLHrGTEK	C2(Carbamidomethyl); R11(Dimethyl)	Control, R25, R50, M50, P25, P50
		ETAHWKPPPwNDVDVLK	W10(Oxidation)	25
D3ZG43	NDUFS3	FDLNSPwEAFPAYR	W7(Oxidation)	Control, R25
		FDLNSPwEAFPAYR	W7(Dioxidation)	R25, M25
Q5XIF3	NDUFS4	HGwSYDVEGR	W3(Dioxidation)	R25, R50
		HGwSYDVEGR	W3(Oxidation)	R25, R50
		SYGANFSwNKR	W8(Dioxidation)	R25, M25, P50
		SYGANFSwNKR	W8(Oxidation)	R25, R50
D3ZCZ9	NDUFS6	IIAcDGGGGALGHPK	C4(Trioxidation)	Control, R50, M25, P25, P50
Q5RJN0	NDUFS7	LDDLINwAR	W7(Dioxidation)	Control, R25, R50, M25, P25, P50
		DDLINwAR	W7(Oxidation)	R25, M25, P50
B0BNE6	NDUFS8	ILmwTELFR	M3(Oxidation); W4(Dioxidation)	Control, R25, M25
Q5XIH3	NDUFV1	EGVDwmNK	W5(Dioxidation); M6(Oxidation)	R25, P25, P50
		GDARPAEIDSLwEISK	W12(Dioxidation)	R25, M25, P25, P50
		GDARPAEIDSLwEISK	W12(Oxidation)	R25, M25, P50
		GGTwFAGFGR	W4(Dioxidation)	R25, R50, M25
		GGTwFAGFGR	W4(Oxidation)	R25
		GPDwILGEmK	W4(Dioxidation); M9(Oxidation)	R25, R50, M50
		GPDwILGEmK	W4(Oxidation); M9(Oxidation)	R25, R50, M50
		LKPPFPADVGVFGcPTTVANVET-VAVSPTIcR	C14(Carbamidomethyl); C31(Trioxidation)	R25, P50
		QIEGHTIcALGDGAAwPVQGLIR	C8(Carbamidomethyl); W16(Dioxidation)	R25, M25
		QIEGHTIcALGDGAAwPVQGLIR	C8(Carbamidomethyl); W16(Oxidation)	R25, R50, M25
		YLVVNADEGEPGTcKDR	C14(Trioxidation)	R25
		EGVDwMNK	W5(Oxidation)	R50, M50, P25
G3V644	NDUFV3	GPELEwK	W6(Oxidation)	Control, R25, M25
D2E6K0	ND4	IIFPSIMLLPLTwLSANK	W13(Dioxidation)	R25, M25, P25, P50
A0A096XKT9	ND5	LSLNLLDLIwLEK	W10(Dioxidation)	Control, R25, M25, P25, P50
		LSLNLLDLIwLEK	W10(Oxidation)	R25, M25, P25, P50

(Fig. 1D and E), that were associated with cell death pathways, mitochondrial proteins, structural changes, calcium and antioxidant function among others (Fig. 2). Mitochondrial proteins with altered expression included CI subunits (NDUFA10-l1, NDUFS1, NDUFS5-6), cytochrome C oxidase subunits, other metabolic proteins (Table 1) and altered cytoskeletal proteins (vimentin, caldesmon) (Table 1). Our study also showed altered expression of aminoacyl tRNA biosynthesis proteins (Table 1), highlighted in a previous study [26].

Among the antioxidant proteins, Superoxide dismutase-2 (SOD2) ubiquitously expressed in the brain [39] showed down-regulation (Table 1), which could contribute to oxidative damage [39] and neurodegeneration as noted in PD patients [40].

Structural changes induced by the toxins included altered expression of cytoskeletal proteins altered such as vimentin and the actin-binding Caldesmon (Fig. 2 and Table 1), necessary for mitochondrial trafficking in neurons [41] as noted in neurodegenerative diseases including PD [42]. Similarly, Caveolin-1, involved in endocytosis regulates synaptic remodeling and transmission and neurotrophic signaling [43–45], with a role in ageing was downregulated in the three models in our study (Table 1). Loss of caveolin-1 enhanced oxidative stress and neurodegeneration as previously noted [46, 47].

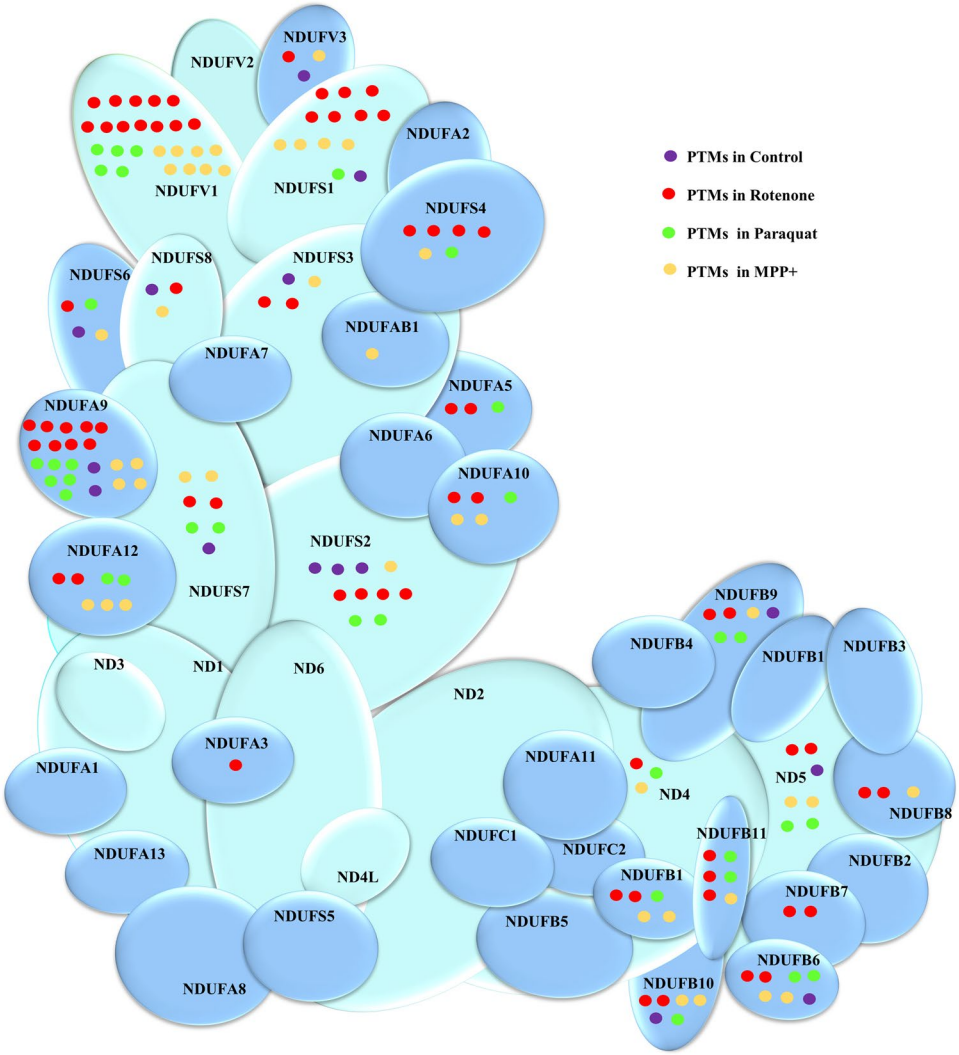

Fig. 5 Distribution PTMs in different subunits of CI. Schematic representation of mammalian CI structure, showing the distribution of PTMs [mono-, di-, tri-oxidation (Trp, Cys), Cysteinyl (C) and dimethyl (R)] across different subunits in control, Rot, Pq and MPP^+ are shown. The names of different subunits of CI (Core subunits in light blue and supernumerary subunits in dark blue) and their arbitrary location in the complex are indicated. The number of filled circles in each subunit correspond to the number of PTMs detected and the colour of the filled circle corresponds to the particular experimental group (control, Rot, Pq and MPP^+)

Calcium binding proteins are necessary to maintain physiological calcium levels and regulate excitotoxicity [48, 49]. The Ca^{2+}-binding protein S100A4, involved in modulating various cellular functions [50], was overexpressed in all three models (Fig. 2 and Table1). The neuroprotective role of S100A4 in PD has been demonstrated [51], although its neurotoxic role is currently unknown.

The role of Dual specificity phosphatase (DUSPs) in protein phosphorylation dynamics is noted in CNS disease [52, 53] and their altered expression might play an essential role in PD pathogenesis [54]. Our study showed overexpression of DUSPs in all three models (fold change 1.69–2.81) with implications for PD.

The overview of the proteomic data highlighted the similarity among the downstream pathways in the three neurotoxic models. This could be due to the fact that the three toxins target CI and potentially induce oxidative stress and mitochondrial damage. We believe that since mitochondrial dysfunction is connected to metabolic changes including ETC and oxidative phosphorylation, altered calcium and redox dynamics and could be linked to cell death pathways, they could form a cascade leading to neurodegeneration. However, the chronology of these events is not clearly understood since some pathways could work synergistically to exacerbate the neurotoxic effect.

Structural Implications of Protein Oxidation in CI

The optimal protein conformation of cellular proteins could be influenced by PTMs. Oxidative PTMs alter the structure–function relationship of proteins and contribute to ageing and neurodegeneration [55]. Oxidative and nitrative modifications have been reported in human samples and experimental models of neurodegenerative diseases such as PD and Alzheimer's disease (AD), which includes reversible modifications such as cysteine oxidation [56, 57]. Danielson et al. [58] reported quantification of reversible oxidation of 34 distinct cysteine residues out of a total 130 present

Table 5 List of CI PTMs identified in this study that were common to the previous studies. The subunit symbol, annotated peptide sequence [modified residues in lower case], the amino acid (AA) position in the protein, specific PTM and reference are shown

No	Subunit	Annotated Sequence	PTMs	Reference
1	NDUFA5	mLQWKPWEPLVEEPPANQwK	M1(Oxidation); W19(Dioxidation)	[22]
2	NDUFA5	TTGLVGLAVcDTPHER	C10(Trioxidation)	[22]
3	NDUFA9	LFGLSPFEPwTTK	W10(Dioxidation)	[22]
4	NDUFB7	DSFPNFVAcK	C9(Trioxidation)	[63]
5	NDUFV1	GDARPAEIDSLwEISK	W12(Dioxidation)	[22]
6	NDUFV1	GPDwILGEmK	W4(Dioxidation); M9(Oxidation)	[22]
7	NDUFV1	LKPPFPADVGVFGcPTTVANVET-VAVSPTIcR	C14(Carbamidomethyl); C31(Trioxidation)	[58]
8	NDUFV1	YLVVNADEGEPGTcKDR	C14(Trioxidation)	[58]
9	NDUFS1	GLLTYTSwEDALSR	W8(Dioxidation)	[22]
10	NDUFS2	KcDPHIGLLHrGTEK	C2(Carbamidomethyl); R11(Dimethyl)	[82, 83]
11	NDUFS3	FDLNSPwEAFPAYR	W7(Dioxidation)	[22]
12	NDUFS4	SYGANFSwNKR	W8(Dioxidation)	[22]
13	NDUFS6	IIAcDGGGGALGHPK	C4(Trioxidation)	[58]
14	NDUFS7	LDDLINwAR	W7(Dioxidation)	[22]
15	NDUFS8	ILmwTELFR	M3(Oxidation); W4(Dioxidation)	[22]

in murine CI in a glutathione depletion model of PD with structural implications for iron-sulfur clusters highlighting the importance of their redox status in electron transport function. Similarly, the link between redox proteome and protein aggregation in AD pathogenesis has been established [59]. Newman et al. [60] demonstrated a significant increase in S-glutathionylated proteins in the AD human brain samples via redox proteomic approach highlighting the importance of reversible cysteine proteomic changes in neurodegeneration.

CI is a major target for protein oxidation-mediated inhibition of enzyme activity [6]. MS of CI subunits have identified PTMs including (1) glutathionylation of the 75 kDa subunit (Cys^{531} and Cys^{704}) [61], (2) oxidation of NDUFS1 (Cys^{92}, Cys^{463}, and Cys^{554}), NDUFS2 (Cys^{347}), NDUFS7 (Cys^{59} and Cys^{80}) [58] (3) oxidation of B17.2 (Trp^{61}) [62] (4) dioxidation of tryptophan in NDUFV1, NDUFA5, NDUFA9, NDUFS1, NDUFS2, NDUFS4, NDUFS7, and NDUFS8 [63] (5) nitration of B14 (Tyr^{122}), B15 (Tyr^{46}, Tyr^{50}, and Tyr^{51}) [62] (6) phosphorylation of MWFE (Ser^{55}) [64] (7) dimethylation of 49 kDa subunit (Arg^{85}) [64] and (8) hydroxylation of PSST subunit (Arg^{77}) [64].

Several amino acids are vulnerable to oxidation with Cys and Trp among the frequently oxidized amino acids. Trp oxidation generates three species: oxindolylalanine (with increased mass of + 16 Da over Trp), N-formylkynurenine (+ 32 Da), and kynurenine (+ 4 Da). It should be noted that Trp oxidation in a peptide is a specific event and is dependent on the neighboring residues [65]. However, sample preparation is critical to identify Trp oxidation since methods using gel electrophoresis could generate false-positive Trp oxidative PTMs [65]. This point is not applicable to the current study since we have employed only in-solution methods.

Studies have reported Trp oxidation in mitochondrial proteins under physiological conditions. Taylor et al. [63] identified Trp oxidation in the CI subunits NDUFV1 and NDUFA9. Our previous studies reported Trp oxidation in mitochondrial proteins in mouse models and human samples of muscle pathologies [7]. MS analysis of CI in the current study detected widespread Trp oxidation among CI subunits (Fig. 3F and Table 5), with Rot model displaying relatively higher number of oxidation events compared to the other two models.

None of the studies till date have assessed the structural effects of Trp oxidation on CI. Rat CI has 161 Trp residues across all the subunits, among which 62 residues were oxidized in all three neurotoxic models (Fig. 3C and Table 5). The peripheral arm of CI showed higher number of oxidized Trp compared to the membrane arm (Fig. 3F and Table 5), with NDUFV1 displaying the maximum number of oxidized Trp residues compared to other subunits. We noted that the Trp residues which are susceptible to oxidation were located either at the end of the secondary structure or in an open loop and were either completely or partially exposed to the solvent, and were surrounded by nonpolar amino acids [7].

CI structure facilitates electron transfer and proton translocation [66]. Mutations in CI subunits are linked with mitochondrial diseases [67]. Since, the subunit organization is critical to generate a physiologically functional CI [68], mutations and PTMs could alter the structure–function relationship [6, 55]. Structural alterations in one subunit could induce structural changes in other

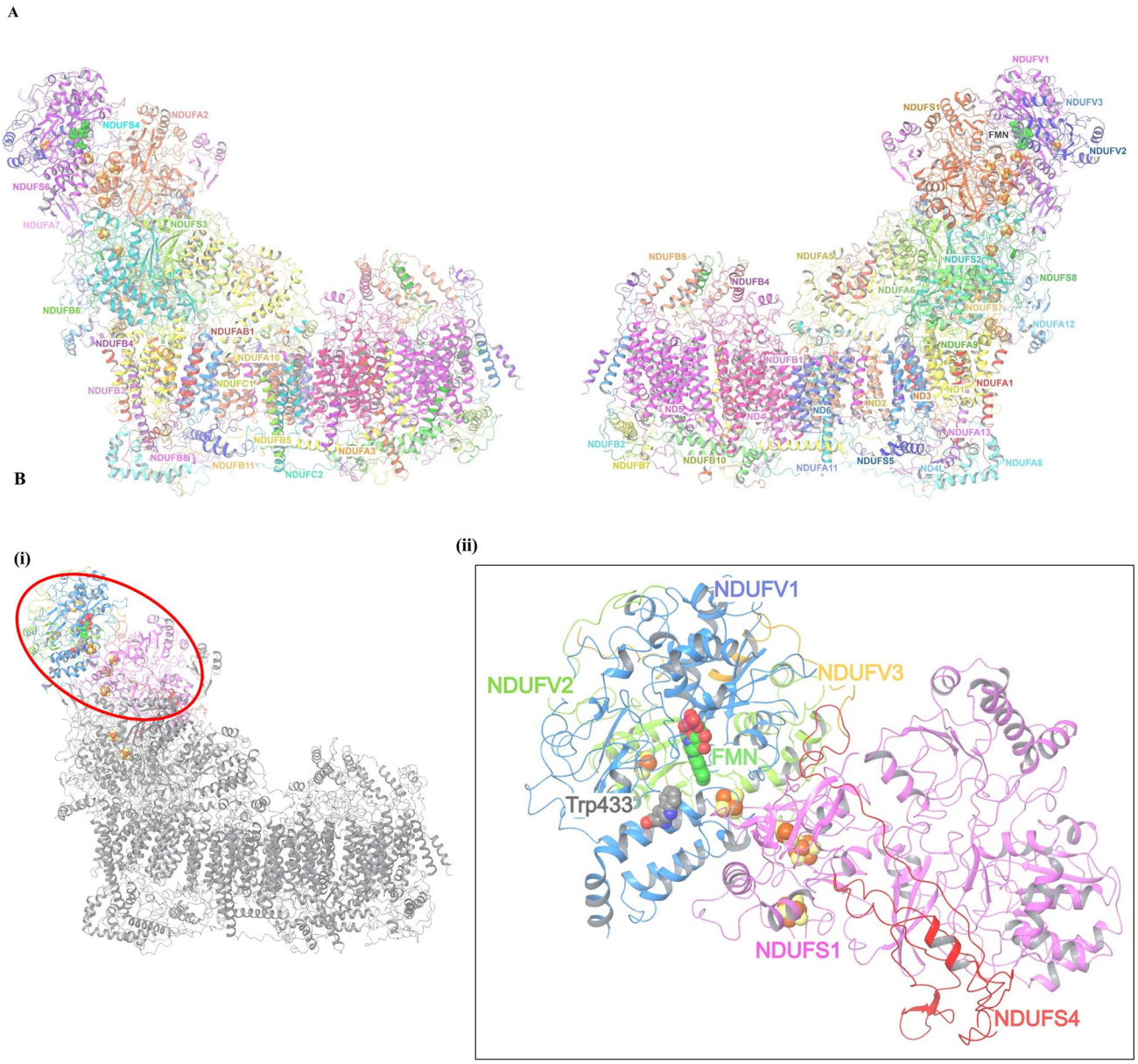

Fig. 6 Homology modeling of rat CI. **A** Homology modeling of Rat CI built using mouse model (PDB: 6G2J) as a template. The structure shows 44 subunits of the complex (each labelled with the constituent helices shown in different colours), FMN co-factor (green) and Fe-S clusters (yellow-orange). **B** Enlarged view of CI sub-complex considered for the molecular dynamics study. The five subunits of the sub-complex consisting of NDUFV1(blue), NDUFV2(green), NDUFV3 (yellow), NDUFS1 (pink) and NDUFS4 (red) are shown. The co-factor (FMN) and Fe-S clusters (yellow-orange) along with the Trp433 of NDUFV1 targeted for oxidation are shown

subunits of the complex. For e.g., our previous MDS study demonstrated that oxidation of Trp395 in UQCRC1 subunit of CIII caused structural changes in the other subunits, thereby altering the flexibility of the complex, potentially impairing the electron transfer [69]. Subtle structural changes could have profound effect on protein function. This is exemplified by the optimal distance between consecutive Fe-S clusters in CI, which is critical for its activity. Our previous MDS analysis in CI subunits NDUFV1, NDUFS1 and NDUFV2 showed that phosphorylation induced local structural alterations, thereby altering the efficiency of electron transfer from FMN, ultimately affecting the CI activity [70]. The optimal distance between successive Fe-S in protein complexes is ~14 Å [71]. In CI, the electron transfer from NADH to ubiquinone requires the presence of at least seven Fe-S clusters (N1b, N2, N3, N4, N5, N6a and N6b), that form a ~95 Å long chain of redox centers [72]. Altered distance between consecutive Fe-S clusters, either delays the electron transfer or causes a short-circuit [73].

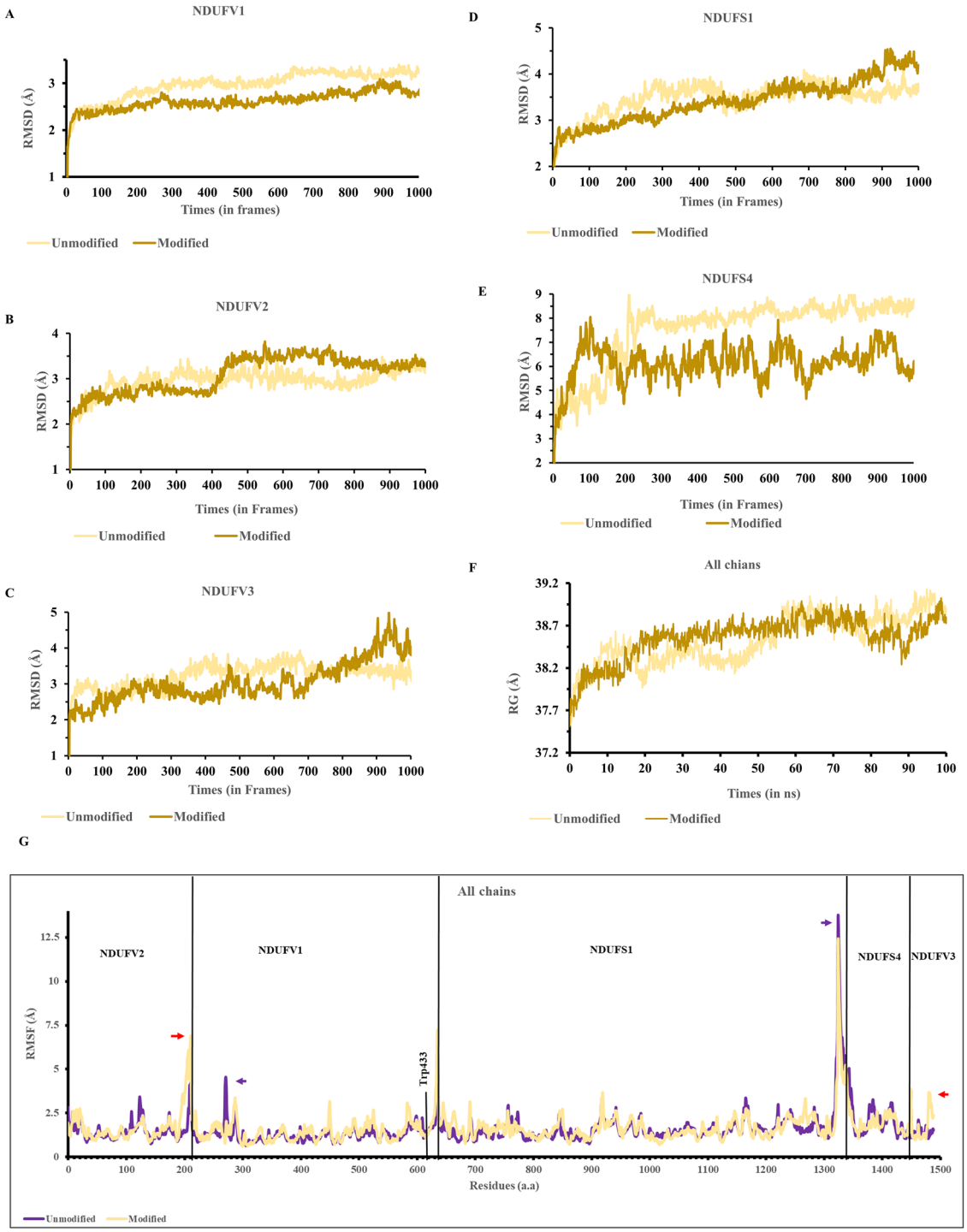

Fig. 7 Molecular dynamics simulation (MDS) of CI subcomplex. RMSD of all 5 chains **A** NDUFV1, **B** NDUFV2, **C** NDUFV3, **D** NDUFS1 and **E** NDUFS4 is shown. The RMSD curves the unmodified and modified (Trp 433) chains are shown in different colours. The Rg of all the five chains of the CI subcomplex is shown in (**F**). **G** RMSF of all 5 Chains with modified Trp433 (dark yellow) and unmodified (light yellow), are shown. The RMSF of each subunit is demarcated from the next by a solid line. The RMSF corresponding to Trp433 is indicated. The significant increase and decrease in RMSF (in A^o) of the modified subcomplex is indicated by red and blue arrows respectively

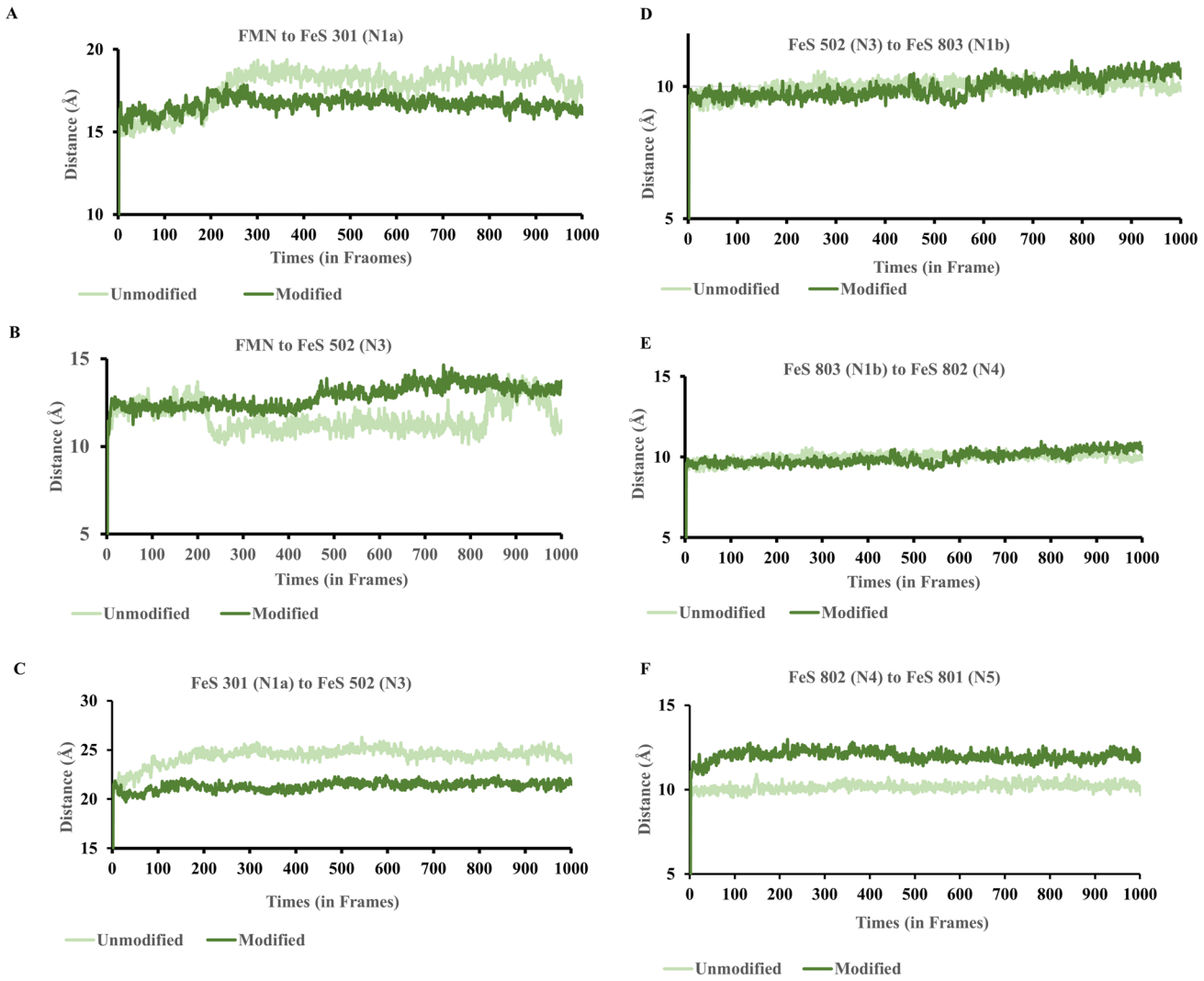

Fig. 8 Distance analysis between FMN and the first 5 consecutive Fe-S clusters based on MDS data. Distance between **A** FMN to FeS 301 residues, **B** FMN to FeS 502 (N3), **C** FeS 301 (N1a) to FeS 502 (N3), **D** Fes 502 (N3) to FeS 803 (N1b), **E** FeS 803 (N1b) to FeS 802 (N4), **F** FeS 802 (N4) to FeS 801 (N5) in unmodified (light green), and Trp433 modified (dark green) subcomplexes and are shown. The distance (shown in A^{o}) between FMN and first five consecutive Fe-S clusters within the sub-complex in both unmodified and Trp433 modified conditions at **G** 0 ns, **H** 50 ns and **I** 100 ns are shown

Considering the technical limitation in carrying out MDS on the entire CI, we generated an unmodified and modified sub-complex containing five peripheral arm subunits that interact with FMN site and Fe-S clusters. MDS data revealed that PTM at W433 altered the arrangement of Fe-S clusters as indicated by the decreased distance between Fe-S 301 (N1a) to Fe-S 502 (N3) and increased distance between Fe-S 802 (N4) to Fe-S 801 (N5) at 100 ns (Fig. 8C, F and I). Other structural changes included decreased hydrogen bonding between NDUFV1-NDUFS1 and NDUFV1-NDUFS4 (Fig. 9C and D) and altered hydrogen bonding between Trp433 and Gly437 (Fig. 9I). We are tempted to speculate that local conformational changes could probably contribute to altered structure–function relationship of the complex. However, such studies have certain limitations. Firstly, the study was not carried out on the entire complex. Secondly, we have not considered all the PTMs across of CI. Whether these structural changes are noted during the disease progression in the human brain needs to be considered for clinical implications of PD. Further, assessment of other oxidative mechanisms including protein carbonylation, cysteine oxidation could provide additional information about the neurotoxic mechanisms at the protein level, although we have not conducted any quantitative proteomics in these models to ascertain the same. It is possible that regulation of cysteine redox proteome on its own or following Trp oxidation could have structural implications for CI

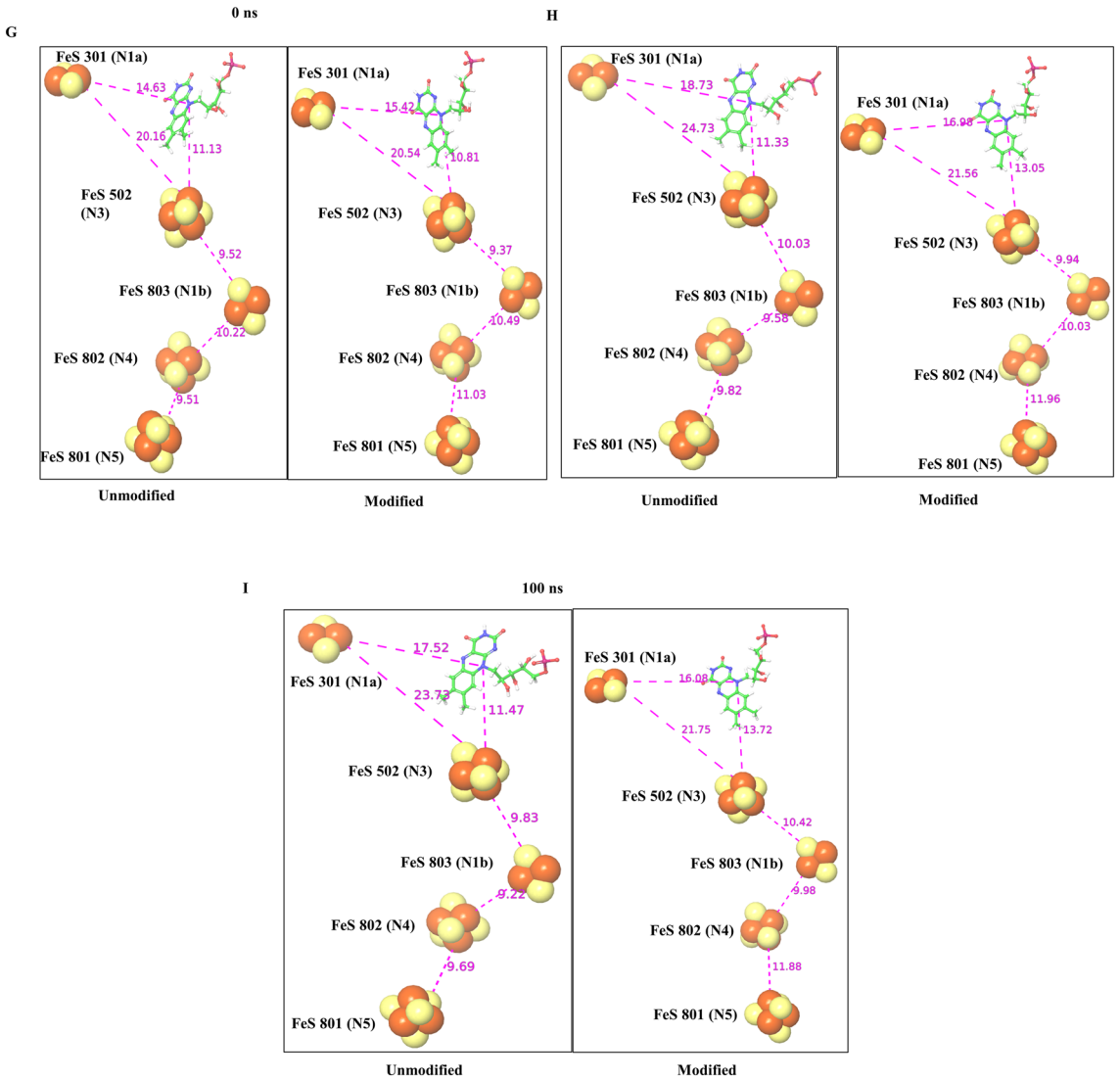

Fig. 8 (continued)

in particular and functional implications for mitochondrial function in general.

Considering that oxidative stress and protein oxidation have potential structural and functions effects on mitochondrial function including CI, antioxidants such as n-acetyl cysteine have antioxidant and neuroprotective potential with therapeutic implications for neurodegeneration and Parkinson's disease. Our previous studies have demonstrated that natural antioxidants such as curcumin and their derivatives have neuroprotective effects against mitochondrial dysfunction, CI dysfunction and oxidative damage using in vitro and in vivo models [10, 13, 74–76]. Similarly, soluble extract from Bacopa monnieri has been tested for their antioxidant and neuroprotective effects in neurotoxic models in vivo [77–80] with implications for neurodegenerative diseases.

To our knowledge, this is one of the first studies that has combined analysis of downstream pathways induced by the CI specific toxins along with the assessment of the structural changes induced by the PTMs in these models. This could provide insights not only into the function of CI but also highlight the critical residues important for the catalytic activity, that are targeted for oxidative PTMs in the neurotoxic models.

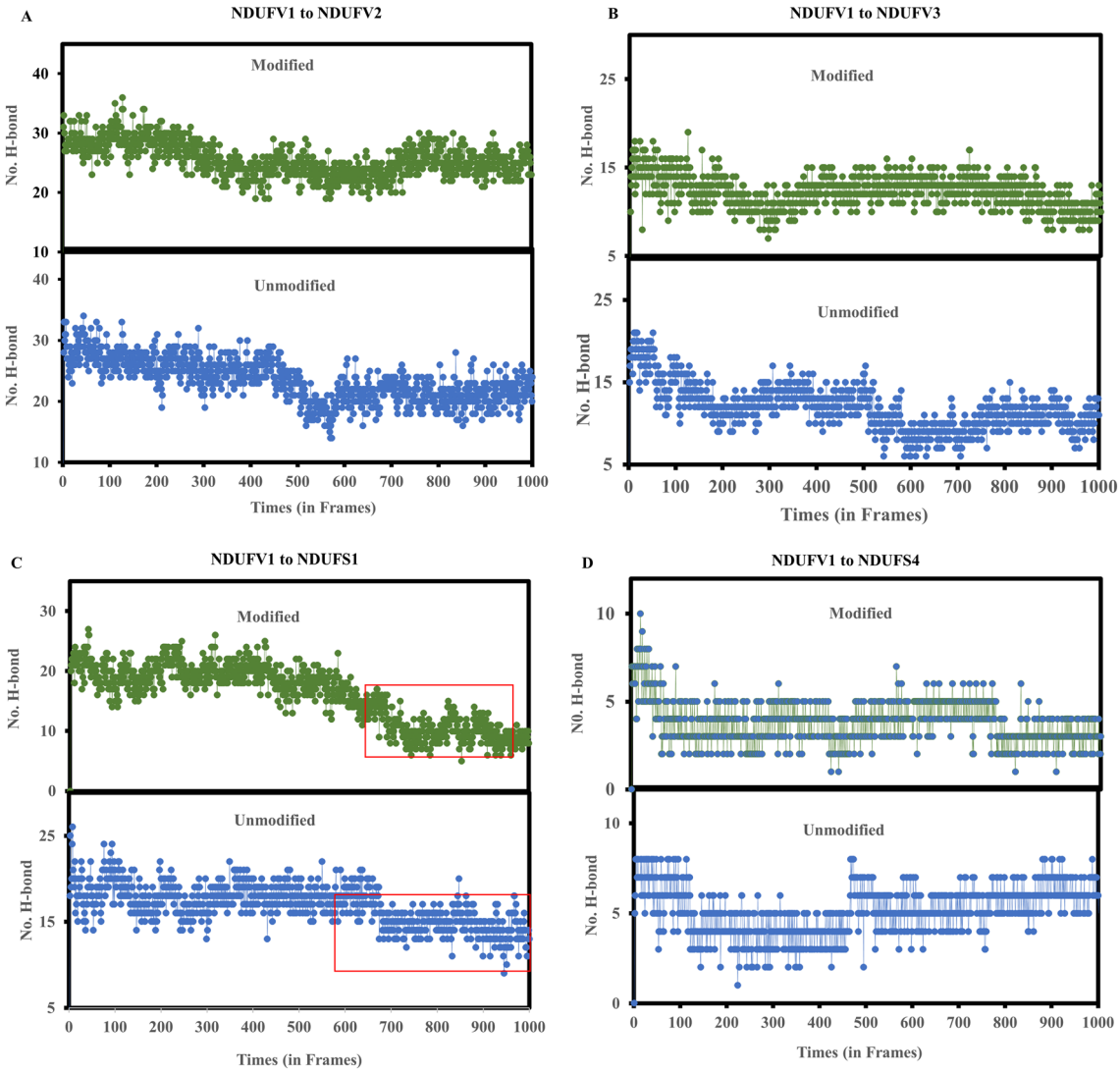

Fig. 9 Hydrogen bond analysis at subunit and residues level of the subcomplex: The number of hydrogen bonds measured in unmodified (blue) and Trp433 modified (Green) CI subcomplex between **A** NDUFV1 and NDUFV2, **B** NDUFV1 And NDUFV3, **C** NDUFV1 and NDUFS1 and **D** NDUFV1 and NDUFS4 are shown. The hydrogen bonding measured at the residue level in the unmodified vs. modified subcomplex between Trp433 and its interacting neighboring residue G430 of NDUFV1 is shown in (**E**). The distance between Trp433 and Gly430 (**F**) and between Trp433 and Gly437 **G** in both unmodified (yellow) and Trp433 modified sub-complex (green) are shown (The hydrogen bond data between Trp433 and Gly437 are not shown). Pymol structures of the distances (between W433 and its neighboring residues G30 and G437 at **H** 0 ns **I** 50 ns and **J** 100 ns of the MDS experiment are shown. **K–L,** Altered local structure in NDUFV1 showing Trp433 and its neighbouring residues Gly430 and Gly437

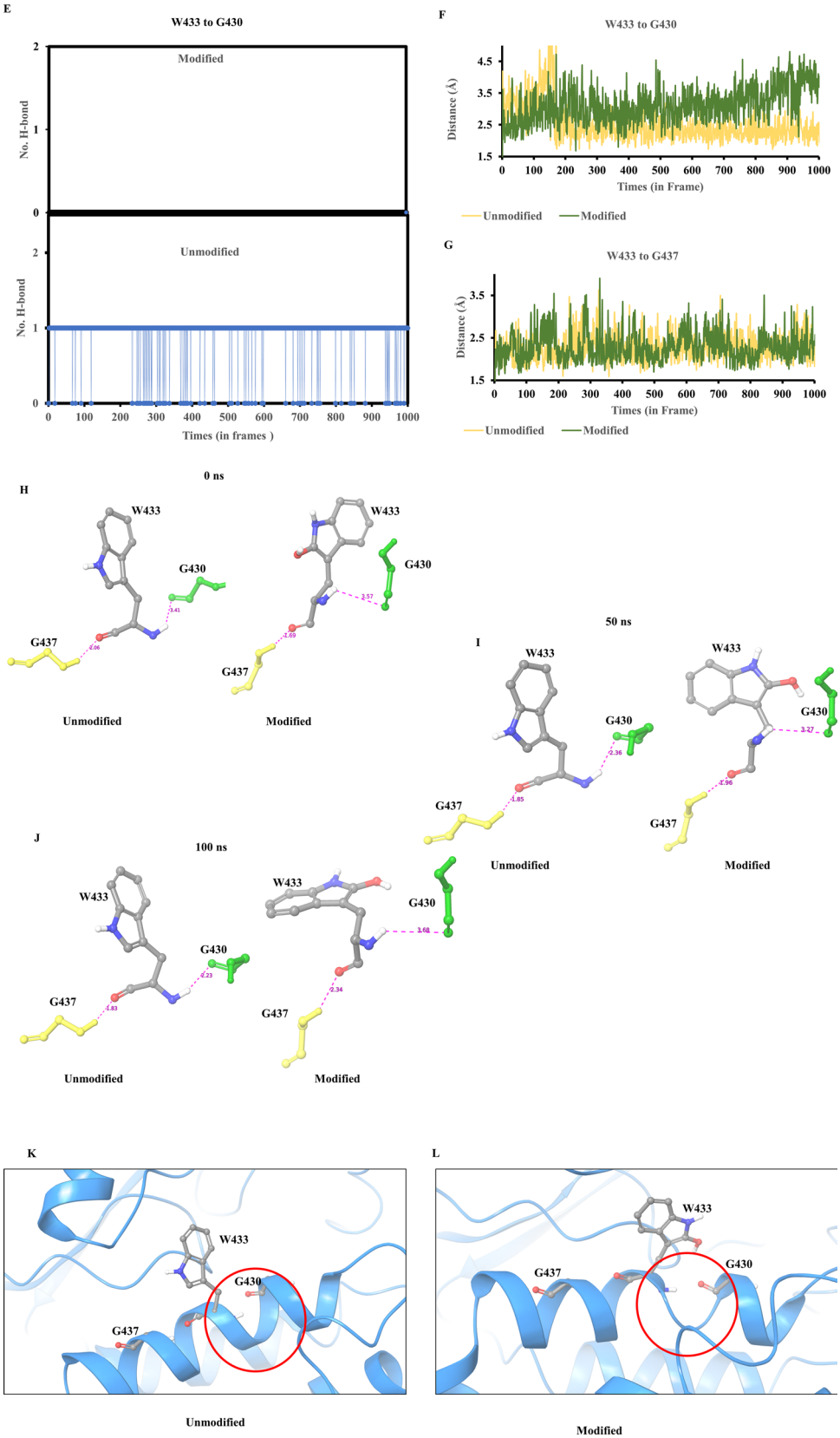

Fig. 9 (continued)

Supplementary Information The online version contains supplementary material available at https://doi.org/10.1007/s11064-023-03907-x.

Acknowledgements This study was supported by the institutional funds allocated to the Department of Clinical Psychopharmacology and Neurotoxicology, NIMHANS. The technical help provided by Vismaya Meghalamane regarding Complex I proteomics experiments is gratefully acknowledged.

Author contributions Y.C. carried out the experiments, analyzed the data and wrote the first draft of the manuscript. G.D. and V.G. contributed to the mass spectrometry experiments including data analysis. V.C. contributed to the Molecular Dynamics Simulation and preparation of related figures. NG contributed to proteomic data analysis and PTM analysis. V.V. supervised the research study. M.M.S.B. designed and supervised the study, analyzed the data, edited and prepared the final version of the manuscript. All the authors approved the final version of the manuscript.

Funding This study was supported by the National Institute of Mental Health and Neurosciences

Data Availability The proteomics (MS) data from this study have been deposited to the ProteomeXchange Consortium via the PRIDE partner repository [81] with the dataset identifier PXD037322.

Declarations

Conflict of interest The authors have no conflict of interest to report.

References

1. Perry TL, Godin DV, Hansen S (1982) Parkinson's disease: a disorder due to nigral glutathione deficiency? Neurosci Lett 33:305–310. https://doi.org/10.1016/0304-3940(82)90390-1
2. Schapira AH, Mann VM, Cooper JM et al (1990) Anatomic and disease specificity of NADH CoQ1 reductase (complex I) deficiency in Parkinson's disease. J Neurochem 55:2142–2145. https://doi.org/10.1111/j.1471-4159.1990.tb05809.x
3. Swerdlow RH, Parks JK, Miller SW et al (1996) Origin and functional consequences of the complex I defect in Parkinson's disease. Ann Neurol 40:663–671. https://doi.org/10.1002/ana.410400417
4. Lazarou M, Thorburn DR, Ryan MT, McKenzie M (2009) Assembly of mitochondrial complex I and defects in disease. Biochim Biophys Acta 1793:78–88. https://doi.org/10.1016/j.bbamcr.2008.04.015
5. Swalwell H, Kirby DM, Blakely EL et al (2011) Respiratory chain complex I deficiency caused by mitochondrial DNA mutations. Eur J Hum Genet 19:769–775. https://doi.org/10.1038/ejhg.2011.18
6. Srinivas Bharath MM (2017) Post-translational oxidative modifications of mitochondrial complex I (NADH: ubiquinone oxidoreductase): implications for pathogenesis and therapeutics in human diseases. J Alzheimers Dis 60:S69–S86. https://doi.org/10.3233/JAD-170117
7. Sunitha B, Gayathri N, Kumar M et al (2016) Muscle biopsies from human muscle diseases with myopathic pathology reveal common alterations in mitochondrial function. J Neurochem 138:174–191. https://doi.org/10.1111/jnc.13626
8. Nandipati S, Litvan I (2016) Environmental exposures and Parkinson's disease. Int J Environ Res Public Health 13:881. https://doi.org/10.3390/ijerph13090881
9. Prasad KN, Carvalho E, Kentroti S et al (1994) Establishment and characterization of immortalized clonal cell lines from fetal rat mesencephalic tissue. In Vitro Cell Dev Biol Anim 30A:596–603. https://doi.org/10.1007/BF02631258
10. Mythri RB, Jagatha B, Pradhan N et al (2007) Mitochondrial complex I inhibition in Parkinson's disease: how can curcumin protect mitochondria? Antioxid Redox Signal 9:399–408. https://doi.org/10.1089/ars.2006.1479
11. Vali S, Mythri RB, Jagatha B et al (2007) Integrating glutathione metabolism and mitochondrial dysfunction with implications for Parkinson's disease: a dynamic model. Neuroscience 149:917–930. https://doi.org/10.1016/j.neuroscience.2007.08.028
12. Chan FK-M, Moriwaki K, De Rosa MJ (2013) Detection of necrosis by release of lactate dehydrogenase activity. Methods Mol Biol 979:65–70. https://doi.org/10.1007/978-1-62703-290-2_7
13. Harish G, Venkateshappa C, Mythri RB et al (2010) Bioconjugates of curcumin display improved protection against glutathione depletion mediated oxidative stress in a dopaminergic neuronal cell line: implications for Parkinson's disease. Bioorg Med Chem 18:2631–2638. https://doi.org/10.1016/j.bmc.2010.02.029
14. Bradford MM (1976) A rapid and sensitive method for the quantitation of microgram quantities of protein utilizing the principle of protein-dye binding. Anal Biochem 72:248–254. https://doi.org/10.1006/abio.1976.9999
15. Rappsilber J, Mann M, Ishihama Y (2007) Protocol for micro-purification, enrichment, pre-fractionation and storage of peptides for proteomics using StageTips. Nat Protoc 2:1896–1906. https://doi.org/10.1038/nprot.2007.261
16. Trounce IA, Kim YL, Jun AS, Wallace DC (1996) Assessment of mitochondrial oxidative phosphorylation in patient muscle biopsies, lymphoblasts, and transmitochondrial cell lines. Methods Enzymol 264:484–509. https://doi.org/10.1016/s0076-6879(96)64044-0
17. Butterfield DA, Stadtman ER (1997) Chapter 7 protein oxidation processes in aging brain. In: Timiras PS, Bittar EE (eds) Advances in cell aging and gerontology. Elsevier, pp 161–191
18. Ryan K, Backos DS, Reigan P, Patel M (2012) Post-translational oxidative modification and inactivation of mitochondrial complex I in epileptogenesis. J Neurosci 32:11250–11258. https://doi.org/10.1523/JNEUROSCI.0907-12.2012
19. Schneider CA, Rasband WS, Eliceiri KW (2012) NIH Image to ImageJ: 25 years of image analysis. Nat Methods 9:671–675. https://doi.org/10.1038/nmeth.2089
20. Vanommeslaeghe K, Hatcher E, Acharya C et al (2010) CHARMM general force field: a force field for drug-like molecules compatible with the CHARMM all-atom additive biological force fields. J Comput Chem 31:671–690. https://doi.org/10.1002/jcc.21367
21. Zeng X-S, Geng W-S, Jia J-J (2018) Neurotoxin-induced animal models of Parkinson disease: pathogenic mechanism and assessment. ASN Neuro 10:1759091418777438. https://doi.org/10.1177/1759091418777438
22. Mythri RB, Raghunath NR, Narwade SC et al (2017) Manganese- and 1-methyl-4-phenylpyridinium-induced neurotoxicity display differences in morphological, electrophysiological and genome-wide alterations: implications for idiopathic Parkinson's disease. J Neurochem 143:334–358. https://doi.org/10.1111/jnc.14147
23. Mohankumar T, Chandramohan V, Lalithamba HS et al (2020) Design and molecular dynamic investigations of 7,8-dihydroxyflavone derivatives as potential neuroprotective agents against

alpha-synuclein. Sci Rep 10:599. https://doi.org/10.1038/s41598-020-57417-9
24. Zurita Rendón O, Silva Neiva L, Sasarman F, Shoubridge EA (2014) The arginine methyltransferase NDUFAF7 is essential for complex I assembly and early vertebrate embryogenesis. Hum Mol Genet 23:5159–5170. https://doi.org/10.1093/hmg/ddu239
25. Maiti P, Manna J, Dunbar GL (2017) Current understanding of the molecular mechanisms in Parkinson's disease: targets for potential treatments. Transl Neurodegener 6:28. https://doi.org/10.1186/s40035-017-0099-z
26. van Dijk KD, Berendse HW, Drukarch B et al (2012) The proteome of the locus ceruleus in Parkinson's disease: relevance to pathogenesis. Brain Pathol 22:485–498. https://doi.org/10.1111/j.1750-3639.2011.00540.x
27. Basso M, Giraudo S, Corpillo D et al (2004) Proteome analysis of human substantia nigra in Parkinson's disease. Proteomics 4:3943–3952. https://doi.org/10.1002/pmic.200400848
28. Tribl F, Gerlach M, Marcus K et al (2005) "Subcellular proteomics" of neuromelanin granules isolated from the human brain. Mol Cell Proteom 4:945–957. https://doi.org/10.1074/mcp.M400117-MCP200
29. Palacino JJ, Sagi D, Goldberg MS et al (2004) Mitochondrial dysfunction and oxidative damage in parkin-deficient mice. J Biol Chem 279:18614–18622. https://doi.org/10.1074/jbc.M401135200
30. Periquet M, Corti O, Jacquier S, Brice A (2005) Proteomic analysis of parkin knockout mice: alterations in energy metabolism, protein handling and synaptic function. J Neurochem 95:1259–1276. https://doi.org/10.1111/j.1471-4159.2005.03442.x
31. Poon HF, Frasier M, Shreve N et al (2005) Mitochondrial associated metabolic proteins are selectively oxidized in A30P alpha-synuclein transgenic mice–a model of familial Parkinson's disease. Neurobiol Dis 18:492–498. https://doi.org/10.1016/j.nbd.2004.12.009
32. Heeman B, Van den Haute C, Aelvoet S-A et al (2011) Depletion of PINK1 affects mitochondrial metabolism, calcium homeostasis and energy maintenance. J Cell Sci 124:1115–1125. https://doi.org/10.1242/jcs.078303
33. Yao Z, Gandhi S, Burchell VS et al (2011) Cell metabolism affects selective vulnerability in PINK1-associated Parkinson's disease. J Cell Sci 124:4194–4202. https://doi.org/10.1242/jcs.088260
34. Triplett JC, Zhang Z, Sultana R et al (2015) Quantitative expression proteomics and phosphoproteomics profile of brain from PINK1 knockout mice: insights into mechanisms of familial Parkinson's disease. J Neurochem 133:750–765. https://doi.org/10.1111/jnc.13039
35. Karthikkeyan G, Najar MA, Pervaje R et al (2020) Identification of molecular network associated with neuroprotective effects of Yashtimadhu (*Glycyrrhiza glabra* L.) by quantitative proteomics of rotenone-induced Parkinson's disease model. ACS Omega 5:26611–26625. https://doi.org/10.1021/acsomega.0c03420
36. Gielisch I, Meierhofer D (2015) Metabolome and proteome profiling of complex I deficiency induced by rotenone. J Proteome Res 14:224–235. https://doi.org/10.1021/pr500894v
37. Ranganayaki S, Jamshidi N, Aiyaz M et al (2021) Inhibition of mitochondrial complex II in neuronal cells triggers unique pathways culminating in autophagy with implications for neurodegeneration. Sci Rep 11:1483. https://doi.org/10.1038/s41598-020-79339-2
38. Beal MF (2003) Mitochondria, oxidative damage, and inflammation in Parkinson's disease. Ann N Y Acad Sci 991:120–131. https://doi.org/10.1111/j.1749-6632.2003.tb07470.x
39. De Lazzari F, Bubacco L, Whitworth AJ, Bisaglia M (2018) Superoxide radical dismutation as new therapeutic strategy in Parkinson's disease. Aging Dis 9:716–728. https://doi.org/10.14336/AD.2017.1018
40. Flynn JM, Melov S (2013) SOD2 in mitochondrial dysfunction and neurodegeneration. Free Radic Biol Med 62:4–12. https://doi.org/10.1016/j.freeradbiomed.2013.05.027
41. Sheng Z-H (2014) Mitochondrial trafficking and anchoring in neurons: new insight and implications. J Cell Biol 204:1087–1098. https://doi.org/10.1083/jcb.201312123
42. Lippolis R, Siciliano RA, Pacelli C et al (2015) Altered protein expression pattern in skin fibroblasts from parkin-mutant early-onset Parkinson's disease patients. Biochim Biophys Acta 1852:1960–1970. https://doi.org/10.1016/j.bbadis.2015.06.015
43. Suzuki S, Numakawa T, Shimazu K et al (2004) BDNF-induced recruitment of TrkB receptor into neuronal lipid rafts: roles in synaptic modulation. J Cell Biol 167:1205–1215. https://doi.org/10.1083/jcb.200404106
44. Bhatnagar A, Sheffler DJ, Kroeze WK et al (2004) Caveolin-1 interacts with 5-HT2A serotonin receptors and profoundly modulates the signaling of selected Galphaq-coupled protein receptors. J Biol Chem 279:34614–34623. https://doi.org/10.1074/jbc.M404673200
45. Francesconi A, Kumari R, Zukin RS (2009) Regulation of group I metabotropic glutamate receptor trafficking and signaling by the caveolar/lipid raft pathway. J Neurosci 29:3590–3602. https://doi.org/10.1523/JNEUROSCI.5824-08.2009
46. Head BP, Peart JN, Panneerselvam M et al (2010) Loss of caveolin-1 accelerates neurodegeneration and aging. PLoS ONE 5:e15697. https://doi.org/10.1371/journal.pone.0015697
47. Wang S, Wang N, Zheng Y et al (2017) Caveolin-1: an oxidative stress-related target for cancer prevention. Oxid Med Cell Longev 2017:7454031. https://doi.org/10.1155/2017/7454031
48. Surmeier DJ, Guzman JN, Sanchez-Padilla J, Schumacker PT (2011) The role of calcium and mitochondrial oxidant stress in the loss of substantia nigra pars compacta dopaminergic neurons in Parkinson's disease. Neuroscience 198:221–231. https://doi.org/10.1016/j.neuroscience.2011.08.045
49. Hurley MJ, Brandon B, Gentleman SM, Dexter DT (2013) Parkinson's disease is associated with altered expression of CaV1 channels and calcium-binding proteins. Brain 136:2077–2097. https://doi.org/10.1093/brain/awt134
50. Donato R (1999) Functional roles of S100 proteins, calcium-binding proteins of the EF-hand type. Biochim Biophys Acta 1450:191–231. https://doi.org/10.1016/s0167-4889(99)00058-0
51. Pankratova S, Klingelhofer J, Dmytriyeva O et al (2018) The S100A4 protein signals through the ErbB4 receptor to promote neuronal survival. Theranostics 8:3977–3990. https://doi.org/10.7150/thno.22274
52. An N, Bassil K, Al Jowf GI et al (2021) Dual-specificity phosphatases in mental and neurological disorders. Prog Neurobiol 198:101906. https://doi.org/10.1016/j.pneurobio.2020.101906
53. Khoubai FZ, Grosset CF (2021) DUSP9, a dual-specificity phosphatase with a key role in cell biology and human diseases. Int J Mol Sci 22:11538. https://doi.org/10.3390/ijms222111538
54. Luo G-R, Chen S, Le W-D (2006) Are heat shock proteins therapeutic target for Parkinson's disease? Int J Biol Sci 3:20–26. https://doi.org/10.7150/ijbs.3.20
55. Berlett BS, Stadtman ER (1997) Protein oxidation in aging, disease, and oxidative stress. J Biol Chem 272:20313–20316. https://doi.org/10.1074/jbc.272.33.20313
56. Butterfield DA, Palmieri EM, Castegna A (2016) Clinical implications from proteomic studies in neurodegenerative diseases: lessons from mitochondrial proteins. Expert Rev Proteom 13:259–274. https://doi.org/10.1586/14789450.2016.1149470
57. Danielson SR, Andersen JK (2008) Oxidative and nitrative protein modifications in Parkinson's disease. Free Radic Biol Med

44:1787–1794. https://doi.org/10.1016/j.freeradbiomed.2008.03.005
58. Danielson SR, Held JM, Oo M et al (2011) Quantitative mapping of reversible mitochondrial Complex I cysteine oxidation in a Parkinson disease mouse model. J Biol Chem 286:7601–7608. https://doi.org/10.1074/jbc.M110.190108
59. Butterfield DA, Boyd-Kimball D (2019) Redox proteomics and amyloid β-peptide: insights into Alzheimer disease. J Neurochem 151:459–487. https://doi.org/10.1111/jnc.14589
60. Newman SF, Sultana R, Perluigi M et al (2007) An increase in S-glutathionylated proteins in the Alzheimer's disease inferior parietal lobule, a proteomics approach. J Neurosci Res 85:1506–1514. https://doi.org/10.1002/jnr.21275
61. Hurd TR, Requejo R, Filipovska A et al (2008) Complex I within oxidatively stressed bovine heart mitochondria is glutathionylated on Cys-531 and Cys-704 of the 75-kDa subunit: potential role of CYS residues in decreasing oxidative damage. J Biol Chem 283:24801–24815. https://doi.org/10.1074/jbc.M803432200
62. Murray J, Taylor SW, Zhang B et al (2003) Oxidative damage to mitochondrial complex I due to peroxynitrite: identification of reactive tyrosines by mass spectrometry. J Biol Chem 278:37223–37230. https://doi.org/10.1074/jbc.M305694200
63. Taylor Oxidative post-translational modification of tryptophan residues in cardiac mitochondrial proteins - PubMed. https://pubmed.ncbi.nlm.nih.gov/12679331/. Accessed 5 Aug 2021
64. Carroll J, Ding S, Fearnley IM, Walker JE (2013) Post-translational modifications near the quinone binding site of mammalian complex I. J Biol Chem 288:24799–24808. https://doi.org/10.1074/jbc.M113.488106
65. Perdivara I, Deterding LJ, Przybylski M, Tomer KB (2010) Mass spectrometric identification of oxidative modifications of tryptophan residues in proteins: chemical artifact or post-translational modification? J Am Soc Mass Spectrom 21:1114–1117. https://doi.org/10.1016/j.jasms.2010.02.016
66. Sazanov LA (2015) A giant molecular proton pump: structure and mechanism of respiratory complex I. Nat Rev Mol Cell Biol 16:375–388. https://doi.org/10.1038/nrm3997
67. Dang Q-CL, Phan DH, Johnson AN et al (2020) Analysis of human mutations in the supernumerary subunits of complex I. Life 10:296. https://doi.org/10.3390/life10110296
68. Mimaki M, Wang X, McKenzie M et al (2012) Understanding mitochondrial complex I assembly in health and disease. Biochim Biophys Acta 1817:851–862. https://doi.org/10.1016/j.bbabio.2011.08.010
69. Unni S, Thiyagarajan S, Srinivas Bharath MM, Padmanabhan B (2019) Tryptophan oxidation in the UQCRC1 subunit of mitochondrial complex III (ubiquinol-cytochrome C reductase) in a mouse model of myodegeneration causes large structural changes in the complex: a molecular dynamics simulation study. Sci Rep 9:10694. https://doi.org/10.1038/s41598-019-47018-6
70. Sunitha B, Kumar M, Gowthami N et al (2020) Human muscle pathology is associated with altered phosphoprotein profile of mitochondrial proteins in the skeletal muscle. J Proteom 211:103556. https://doi.org/10.1016/j.jprot.2019.103556
71. Moser CC, Farid TA, Chobot SE, Dutton PL (2006) Electron tunneling chains of mitochondria. Biochim Biophys Acta 1757:1096–1109. https://doi.org/10.1016/j.bbabio.2006.04.015
72. Tocilescu MA, Zickermann V, Zwicker K, Brandt U (2010) Quinone binding and reduction by respiratory complex I. Biochim Biophys Acta 1797:1883–1890. https://doi.org/10.1016/j.bbabio.2010.05.009
73. Lenaz G, Fato R, Genova ML et al (2006) Mitochondrial Complex I: structural and functional aspects. Biochim Biophys Acta 1757:1406–1420. https://doi.org/10.1016/j.bbabio.2006.05.007
74. Jagatha B, Mythri RB, Shireen Vali MM, Bharath S (2008) Curcumin treatment alleviates the effects of glutathione depletion in vitro and in vivo: therapeutic implications for Parkinson's disease explained via in silico studies. Free Radical Biol Med 44:907–917. https://doi.org/10.1016/j.freeradbiomed.2007.11.011
75. Mythri RB, Harish G, Dubey SK et al (2011) Glutamoyl diester of the dietary polyphenol curcumin offers improved protection against peroxynitrite-mediated nitrosative stress and damage of brain mitochondria in vitro: implications for Parkinson's disease. Mol Cell Biochem 347:135–143. https://doi.org/10.1007/s11010-010-0621-4
76. Mythri RB, Veena J, Harish G et al (2011) Chronic dietary supplementation with turmeric protects against 1-methyl-4-phenyl-1,2,3,6-tetrahydropyridine-mediated neurotoxicity in vivo: implications for Parkinson's disease. Br J Nutr 106:63–72. https://doi.org/10.1017/S0007114510005817
77. Shinomol GK, Bharath MMS, Muralidhara (2012) Neuromodulatory propensity of *Bacopa monnieri* leaf extract against 3-nitropropionic acid-induced oxidative stress: in vitro and in vivo evidences. Neurotox Res 22:102–114. https://doi.org/10.1007/s12640-011-9303-6
78. Shinomol GK, BharathMuralidhara MMS (2012) Pretreatment with *Bacopa monnieri* extract offsets 3-nitropropionic acid induced mitochondrial oxidative stress and dysfunctions in the striatum of prepubertal mouse brain. Can J Physiol Pharmacol 90:595–606. https://doi.org/10.1139/y2012-030
79. Shinomol GK, Mythri RB, Srinivas Bharath MM, Muralidhara (2012) *Bacopa monnieri* extract offsets rotenone-induced cytotoxicity in dopaminergic cells and oxidative impairments in mice brain. Cell Mol Neurobiol 32:455–465. https://doi.org/10.1007/s10571-011-9776-0
80. Shinomol GK, Raghunath N, Bharath MMS, Muralidhara (2013) Prophylaxis with *Bacopa monnieri* attenuates acrylamide induced neurotoxicity and oxidative damage via elevated antioxidant function. Cent Nerv Syst Agents Med Chem 13:3–12. https://doi.org/10.2174/1871524911313010003
81. Perez-Riverol Y, Bai J, Bandla C et al (2022) The PRIDE database resources in 2022: a hub for mass spectrometry-based proteomics evidences. Nucleic Acids Res 50:D543–D552. https://doi.org/10.1093/nar/gkab1038
82. Kang PT, Chen C-L, Lin P et al (2018) Mitochondrial complex I in the post-ischemic heart: reperfusion-mediated oxidative injury and protein cysteine sulfonation. J Mol Cell Cardiol 121:190–204. https://doi.org/10.1016/j.yjmcc.2018.07.244
83. Rhein VF, Carroll J, Ding S et al (2013) NDUFAF7 methylates arginine 85 in the NDUFS2 subunit of human complex I. J Biol Chem 288:33016–33026. https://doi.org/10.1074/jbc.M113.518803